Pore-scale imaging of hydrogen displacement and trapping in porous media

Eike M. Thaysen[1], Ian B. Butler[1], Aliakbar Hassanpouryouzband[1], Damien Freitas[1], Fernando Alvarez-Borges[2], Samuel C. Krevor[3], Niklas Heinemann[1], Robert Atwood[2], Katriona Edlmann[1]*

[1]School of Geoscience, Grant Institute, The King's Buildings, The University of Edinburgh, James Hutton Road, Edinburgh, EH9 3FE, United Kingdom

[2] Diamond Light Source Ltd, Harwell Campus, Didcot OX11 0DE, United Kingdom

[3] Department of Earth Science and Engineering, Imperial College London, London SW7 2AZ, United Kingdom

---

* = corresponding author email, phone number: eike.thaysen@ed.ac.uk, +34 682079236

Abstract

Hydrogen can act as an energy store to balance supply and demand in the renewable energy sector. Hydrogen storage in subsurface porous media could deliver high storage capacities but the volume of recoverable hydrogen is unknown. We imaged the displacement and capillary trapping of hydrogen by brine in a Clashach sandstone cylinder at 2-7 MPa pore fluid pressure using X-ray computed microtomography. Hydrogen saturation obtained during drainage at capillary numbers of $<10^{-7}$ was ~50% of the pore volume and independent of the injection pressure. Fluid configuration in the pore space was indicative of a water wetting system at all conditions. Capillary trapping of hydrogen via snap-off during secondary imbibition at a capillary number of 2.4×10^{-6} systematically increased with pressure, 20%, 24% and 43% of the initial hydrogen trapped at 2, 5 and 7 MPa, respectively. Injection of brine at increasing capillary numbers up to 9.4×10^{-6} reduced capillary trapping. Based on these results, we recommend more shallow, lower pressure sites for future hydrogen storage operations in porous media.

Keywords: geological hydrogen storage, µCT, porous media, recovery, drainage, imbibition

Highlights:

- Hydrogen injectivity and recovery in rock is imaged with x-ray computed micro-CT
- Hydrogen recovery decreases with increasing reservoir depth
- Hydrogen recovery increases with increasing brine flow rate
- Hydrogen trapping occurs via snap-off processes
- Nitrogen is a poor proxy for hydrogen

1. Introduction

The storage of surplus electrical energy could increase the utility of renewable energy sources thereby reducing the environmental impact of energy generation[1, 2]. Storage mediums like batteries, compressed air, capacitors, or flywheels are only applicable for the short-term and small-scale electricity storage[3]. The use of hydrogen (H_2) as an energy vector however could provide long-term storage to balance the intermittent demand and supply challenges affecting renewable methods[3]. Considering the low energy density of H_2[4], storage of H_2 in large storage sites is the only solution for economical, gigawatt to terawatt-scale H_2 storage. Underground storage of H_2 in salt caverns is an established technology[5], yet, only subsurface porous media (saline aquifers and depleted oil and gas fields), can provide TWh storage capacities that could balance seasonal demands[4]. Relative to cavern storage, inter-seasonal storage in porous media is poorly understood and introduces a range of other complexities[2], including potential pore-clogging by microbial growth[6], gas loss out of diffuse lateral boundaries, viscous fingering of H_2 into reservoir brines, residual trapping and possible reactions with the primary formation fluid and reservoir minerals[7-10]. Each of these requires consideration of multiphase flow, transport and reaction[2, 8].

Recent years have seen several studies on H_2 geochemistry[11-13] and the elucidation of many important flow characteristics of H_2 including; Hydrogen relative permeability[14, 15], interfacial tension (IFT)[16, 17], and H_2/brine/rock contact angles[14, 16-24]. Yet, additional data describing the H_2 fluid flow in different porous formations and under varying conditions are vital to make accurate predictions of the H_2 plume development and to define optimum production strategies[8]. Of particular relevance is the degree of capillary trapping, which leads to a reduced volume of recoverable H_2, in this way impacting the economic feasibility of the operation[8]. The capillary forces that control capillary trapping also control the relative permeability[8]. As such studies on residual trapping give insight to a range of crucial input parameters for pore-scale and reservoir H_2 storage models.

The effects of the brine pore fluid pressures and of brine flow rate on capillary trapping of H_2 are hithertho unknown. The brine pore fluid pressure is linked to the reservoir depth via the hydrostatic gradient, hence an investigation of the latter could facilitate the definition of an optimal storage depth for gas recovery. The flowrate affects the capillary number, N_c, via equation 1:

$$N_C = \frac{q \cdot \mu}{\sigma} \tag{1}$$

where q is the flow, μ is the viscosity and σ is the interfacial tension (IFT). As N_c increases, viscous forces dominate capillary forces and capillary trapping of the nonwetting phase decreases[25]. This capillary desaturation with increasing N_c, depends on the rock type[26] and on the kind of nonwetting phase[25] and is observed around critical capillary numbers of 10^{-5} to 10^{-8} [25].

A non-destructive standard technique for visualization and analysis of wetting and non-wetting phase displacement processes in porous media is x-ray micro-computed tomography (μCT)[27]. Pore-scale models are directly reliant on μCT images to build up the basic models for appropriate understanding of gas storage operations[28]. Previously published μCT studies on two-phase flow in porous media involving gas have largely focused on supercritical carbon dioxide (sCO_2) in sandstones and limestones, e.g.[27, 29-34]. Reported saturations of sCO_2 in non-aged (i.e. not wettability altered by exposure to oil or organic acids) water-wet rocks range from 30-60% during drainage and 15-30% during imbibition, at N_{Ca} between 10^{-8} to 10^{-6} and 10^{-8} to 2×10^{-5}, respectively[27, 30, 32-34]. Studies using subcritical, gaseous carbon dioxide (CO_2), which could be more readily compared to H_2, are scarce. Yet, the characteristic trapping curves for sCO_2 and CO_2, which show the residual saturation (S_{nnwr}) as a function of initial saturation (S_{nwi}), are not significantly different[35]. Saturations of nitrogen (N_2) during drainage and imbibition in sandstones with 6-22% porosity is 43-64% and 43%, respectively, at N_C between 1-7x10^{-8} [36, 37]. Carbon dioxide trapping increases at lower pressures due to decreasing water contact angles[38]. Unlike in CO_2 storage, trapping is not desirable in geological H_2 storage as it leads to unrecoverable H_2.

Some observational studies have suggested that H_2 is less wetting on rocks than CO_2[19, 21]. At the time of writing two µCT studies, one micro-model study and one nuclear magnetic resonance (NMR) study on H_2 exist: Al-Yaseri et al. (2022)[39] used NMR to find H_2 S_{nwi} and S_{nwr} of 4% and <2%, respectively, in a Fontainebleau sandstone at 0.4 MPa and ambient temperature. Higgs et al. (2021)[16] µCT-imaged H_2 injection into a 5 mm diameter and 7.6 mm length core of Bentheimer sandstone at pressures of 6.8 to 20.8 MPa and documented decreasing IFT between H_2 and water with increasing pressure (72.5 mN/m at 6.9 MPa to 69.4 mN/m at 20.7 MPa). Jha et al. (2021)[40] conducted a single cycle H_2-brine displacement sequence in a 5 mm diameter and 15 mm length Gosford sandstone, and used µCT to calculate an S_{nwi} of 65% during drainage and a S_{nnwr} of 41% after brine imbibition. Rock samples in Jha et al. (2021)[40] and Higgs et al. (2021)[16] were sufficiently short for capillary end effects to dominate the flow behaviour, where the wetting phase accumulates close to the production face of the core[41]. The experiment by Jha et al. (2021)[40] was performed at ambient pressure and leaves open the question of variations in H_2 wetting and flow behaviour at reservoir conditions[19]. Increasing pore fluid pressures have been reported to increase the gas saturation and pore network connectivity for nitrogen (N_2) in a brine wet, aged Bashijiqike tight sandstone (0.6% gas saturation at 2 MPa versus 43% at 8 MPa)[36]. The effect of N_C increases from 7.7x10^{-7} to 3.8x10^{-4} on the H_2 flow through a sandstone micro-model at 0.5 MPa was investigated by Lysyy et al. (2022)[20] who found that H_2 saturation increased correspondingly from 18% to 79%[20].

In this work, we used µCT to investigate the displacement and capillary trapping of H_2 by brine in 4.7 mm diameter and 54-57 mm length Clashach sandstone cores as a function of gas and brine pore fluid pressure (2-7 MPa) and flow rate (20 to 80 µl min^{-1}, corresponding to H_2 and brine bulk N_C of $1.7\text{-}6.8 \times 10^{-8}$ and $1.2\text{-}9.4 \times 10^{-6}$, respectively). We show that the H_2 S_{nwi} is independent of pore fluid pressure but that higher brine pore fluid pressures during secondary imbibition increase capillary trapping of H_2, indicating increased trapping at elevated reservoir depths. Higher flowrates during secondary imbibition on the other hand decrease capillary trapping. Our work advances the current understanding of H_2 flow in porous media by delivering the first realistic estimates on how much H_2 can be recovered from the subsurface after injection, disregarding any H_2 loss by microbial or geochemical reactions, as a function of reservoir depth and flow rate.

2. Materials and Methods

2.1 Core-flooding experiments

We performed non-steady and steady state, two-phase core flooding experiments with H_2 (purity 99.9995 vol.%, BOC Ltd.) and brine (0.5 M CsCl or 2 M KI, Sigma-Aldrich) in a Clashash sandstone (Permian, Aeolian sandstone from near Elgin in Scotland. Clashach composition: ~96 wt.% quartz, 2% K-feldspar, 1% calcite, 1% ankerite[42], porosity 11.1-14.4%[42-44]) at ambient temperature (~293 K). The Clashach sandstone, with its low mineralogical variability, yet still comparably big pore space, was chosen in order to facilitate the visualization of the injected H_2 and the interpretation of the results.

Two types of experiments were carried out: The first set of experiments (from now on referred to as UoE (Univeristy of Edinburgh) experiments) was carried out using the µCT instrument at the University of Edinburgh and were aimed at imaging the displacement and capillary trapping of H_2 by brine as a function of saturation after drainage and imbibition under different experimental conditions. Three UoE experiments were carried out that investigated the effect of injection pressure (2-7 MPa), whereof each was repeated once (UoE exp. 1-3, Table 1). The standard error on the H_2 saturation in the repeated experiments was calculated as the standard deviation devided by the square root of the number of repeated experiments. One UoE experiment looked at the effect of the H_2/brine injection ratio on the H_2 saturation (UoE exp. 4, Table 1). This experiment was carried out to evaluate the effect of H_2 injection into aquifers with different magnitudes of brine flow (hydrodynamic aquifers), and to simulate the far field situation, where H_2 and brine move together. Another UoE experiment investigated the effect of secondary drainage and imbibition (UoE exp. 5, Table 1). UoE exp. 6 used N_2 instead of H_2. This experiment was undertaken in order to compare the flow behaviour of the two gases, which is of relevance because N_2 is sometimes used as an analogue for H_2, e.g. in permeability measurements[11, 15]. Because rearrangement processes in the pore volume were noted previously for N_2[36], UoE exp. 7 (Table 1) was undertaken to examine the stability of H_2 in the rock volume over an experimental duration (10 hours): Ten PV of H_2 were injected into a brine-saturated rock and keeping the pressure constant inside the pressure vessel, with imaging undertaken at the start and after 10 hours. The effect of bulk capillary number on drainage and imbibition was deduced by a comparison of the results from UoE exp. 2 and 5 which used flowrates of 20 and 80 µl min^{-1}, respectively, and 5 MPa injection pressure (Table 1).

The second type of experiment (from now on referred to as the ‘dry rock experiment’; Table 1) used synchrotron radiation (Diamond Light Source, I12-JEEP tomography beamline) to capture the time-resolved displacement of H_2 by brine in a dry, H_2-saturated rock. This experiment served as a base of comparison to the displacements of H_2 in wet, brine-saturated rock (UoE experiments).

All experiments used a bespoke x-ray transparent core holder for a 5 mm diameter rock core,

Table 1: Overview over experiments

Experiment	Type of x-ray source	Description	Sample	H_2/brine injection ratio(s)	Flowrate (µl min^{-1})	Injection Pressure (MPa)	Confining Pressure (MPa)	Pore volumes injected	Repetitions of experiment
UoE exp. 1	laboratory	Primary drainage and imbibition in non-steady state displacements of H_2 and brine	1	-	20	7	9	10	1 entire repetition, 1 repetition on drainage only
UoE exp. 2	laboratory	Primary drainage and imbibition in non-steady state displacements of H_2 and brine	1	-	20	5	9	10	1
UoE exp. 3	laboratory	Primary drainage and imbibition in non-steady state displacements of H_2 and brine	1	-	20	2	9	10	1
UoE exp. 4	laboratory	Simultaneous, steady state injections of H_2 and brine	1	1:4, 1:1, 4:1	20	5	9	10	-
UoE exp. 5	laboratory	Primary and secondary drainage and imbibition in non-steady state displacements of H_2 and brine	1	-	80	5	9	10	-
UoE exp.6	laboratory	Non-steady state displacements of N_2 and brine	1	-	20	5	9	10	-
UoE exp.7	laboratory	H_2 stability	1	-	80	5	9	10	-
Dry rock	synchrotron	Non-steady state, brine injection into dry, H_2 saturated rock	2	-	5	5	10	10	-

which was a scaled-up version of the cell described by Fusseis et al. (2014)[45]. In UoE experiments a carbon-fibre reinforced PEEK pressure vessel was used to permit good x-ray transparency. The dry rock experiment used an aluminium pressure vessel to comply with the health and safety requirements at Diamond Light Source. The specifications of the pressure vessels of PEEK and aluminium were engineered with safety factors of 2 times or more over and above the maximum applied confining pressure (10 MPa; Table 1).

Rock cores for the experiments were obtained by diamond drill coring with a water-flushed chuck, followed by preparation of the core ends by grinding on a lathe. Experiments used a set of four high-pressure pumps (Cetoni Nemesys^{TM}, flowrate range 0.072 nl s^{-1} to 13.76 ml s^{-1}): One for the injection of H_2, one for the injection of brine, one to hold the backpressure and one for the confining pressure (Fig. 1). A bespoke manifold system composed of high-pressure 1/8" and 1/16" 316 stainless steel and 1/16" PEEK tubing (Swagelok, Top Industrie and Cole Parmer, respectively) connected the pumps to the core-flood cell (Fig. 1). Additional pressure transducers (ESI Technology; accuracy 0.1% full-scale) were coupled to the flow system at the inlet and outlet to allow for higher precision pressure monitoring than was possible using the integral pressure gauges in the syringe pumps. Cyclic H_2 and brine injections used a Clashach outcrop sample without further cleaning of 4.7 mm diameter and a relatively long length of 54-57 mm to avoid the influences of capillary end effects[46, 47]. To prevent leakage of H_2 into the confining fluid, the rocks were jacketed in aluminium foil and poluolefin heatshrink tubing and sealed with silicone adhesive between the conical-ended pistons within the pressure vessel. In UoE experiments, a water-wet rock was first saturated with brine (0.5 M CsCl) at a flow rate of 70 µl min^{-1}. Afterwards, H_2 was injected (drainage) into the brine-saturated rock at flow rates of 20-80 µl min^{-1}, based on desired capillary-regime N_C of $1.7\text{-}6.8 \times 10^{-8}$ (The viscosity of H_2 is 9.01 µPa s at 298K and 4.7 MPa[48] and the IFT between H_2 and water is 72.6 mN m^{-1} at 298K and 5 MPa[49, 50]). Subsequently, the brine was reinjected (imbibition) at flow rates of 20-

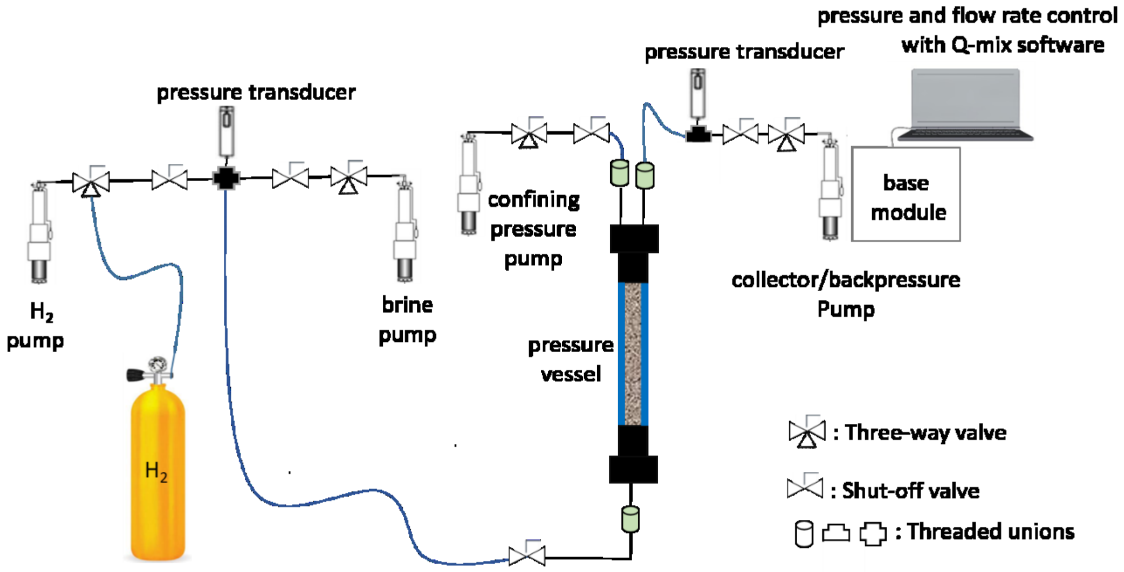

Figure 1: Experimental setup showing the manifold system that connected the X-ray transparent pressure vessel to a set of four high-pressure Cetoni Nemesys^{TM} pumps: one to inject H_2, one inject brine, one to maintain backpressure and one to maintain confining pressure. The materials for the connections were 316 stainless steel (black), HPLC (green) and PEEK or carbon fibre reinforced PEEK (blue). The pressure vessel consisted of carbon fibre reinforced PEEK in UoE experiments and of aluminium in the dry rock experiment (see text). Pressure and flow rate control was achieved with the Q-mix software.

80 µl min^{-1}, resulting in N_C of 2.35-9.45x10^{-6} (using the same IFT between H_2 and water of 72.6 mN m^{-1} at 5 MPa and 298 K[49, 50] and a viscosity of 1.247 Pa s at 5 MPa that was estimated from the reported 1.2503 Pa s and 1.233x10^{-3} Pa s at 0.1 MPa and 25 MPa, respectively, and 298 K[51]). The N_C the N_2 experiment was 3.5x10^{-8} (using an IFT of 73 mN m^{-1} between N_2 and water 1t 298K and 10 MPa[35] and a viscosity of 1.89x10^{-5}Pa s at 5 MPa and 295K[48]). Each injection used ten pore volumes to ensure completely flushing of the sample cores with the injected fluid.

In the dry rock experiment, H_2 was directly injected into a dry rock at a flow rate of 70 µl min^{-1}. Subsequently, the brine (2 M KI) was injected at a flow rate of 5 µl min^{-1}, resulting in N_C of 5x10^{-7} (using the same IFT between H_2 and water of 72.6 mN m^{-1} at 5 MPa and 298 K[49, 50] and a viscosity of 1.07x10^{-3}Pa s for 0.6 M KI and 293 K[42]).

The combined application of an x-ray transparent core holder and μCT allowed the visualization of the fluid saturation distributions at pore scale at each injection step. The difference in the x-ray attenuation coefficient of the fluids (H_2 and 0.5 M CsCl/ 2 M KI) provided an excellent contrast between the two fluid phases and the rock on the acquired μCT images, combined with the respective radiation energy in the two different laboratories.

3D volumes were acquired from the lower central portion of the sample to avoid the impact of capillary end effects on fluid saturation[46, 47]. For the UoE experiments, image acquisition used a μCT instrument built in-house at the University of Edinburgh, comprising a Feinfocus 10-160 kV reflection source, a Micos UPR-160-air rotary table and a Perkin-Elmer XRD 0822 1 MP amorphous silicon flat panel detector with a terbium doped gadolinium oxysulfide scintillator. Data acquisition software was developed in-house. The following settings were used for UoE experiments: 120 keV, 16 W, 2 seconds exposure time, 1200 projections and 2 frames per stop. The voxel size was 5.4 μm^3. In the dry rock experiment, time-resolved imaging of the H_2 and brine displacement processes was achieved by means of a 65 keV monochromatic beam detected by a high-resolution imaging camera with optical module 2 (PCO.edge 5.5, 7.91 x 7.9 μm/pixel with FoV 20 mm x 12 mm) using 17-25 milliseconds exposure time and 900 projections. The voxel size was 7.9 μm^3.

2.2 Image analysis

Tomographic reconstructions were undertaken by filtered back projection using Octopus 8.9[52] on a GPU accelerated workstation. All subsequent image processing and analysis of tomographic data was performed using Avizo Version 9.1.1 (FEI, Oregon, USA). Data from UoE experiments were processed using a non-local means filter[53]. Processing of the dry rock experiment used a combination of median filter and unsharp mask to reduce image noise.Segmentation of UoE experiment data used a global threshold on the 2D greyscale image histogram, and encompassed two phases. In the water-saturated scans, water and rock were treated as two discrete phases. In scans after brine and H_2 injections, the H_2 was treated as one phase and the brine and rock as a single separate phase, following protocols of Andrew et al. (2014)[32]. Holes and spots which were at the resolution limit of the data were removed from all datasets (applied thresholds corresponded to 3^3 and 5^3 voxels, respectively). Based on the segmented image of the water-saturated scan in UoE experiments, a pore size distribution was calculated. The 3D image was separated into individual pores and throats using Avizo's 'separate objects' module, which calculates a chamfer distance map of the pore-space and then applies a marker based watershed algorithm to the distance map to define discrete pore bodies as catchment basins separated by the watershed which marks the location of pore throats (SI Figure S1d). Supporting information Figure S1 shows the work flow for the water-saturated scan.

In scans following brine and H_2 injections in UoE experiments, the segmented image was analysed in 3D using the 'labeling' and 'label analysis' modules to identify, label and measure the volume of each H_2 cluster. Hydrogen cluster size distributions were compared to the pore size distribution to evaluate the H_2 connectivity and identify trapping mechanisms during brine imbibition.

2.3 Capillary pressure

Recovered Clashach cores were submerged in 25% w/v NaOH solution (Fisher Scientific) for 2 hours to remove the aluminium foil from the core surface, and rinsed in successive milli-Q water, acetone and ethanol ultrasonic baths. Subsequently, the cores were cut and squared to the dimensions of 25 mm, overlapping the µCT visualized rock volumes, and cleaned ultrasonically with milli-Q water to remove grinding products. Mercury injection capillary pressure (MICP) was performed on the cleaned cores, using a micromeritics automated mercury injection equipment (Autopore IV 9500) to estimate the capillary pressure-saturation relationship and pore size distribution. The pressure range tested was from vacuum to 379 MPa.

3. Results

3.1 Characterization of the pore space

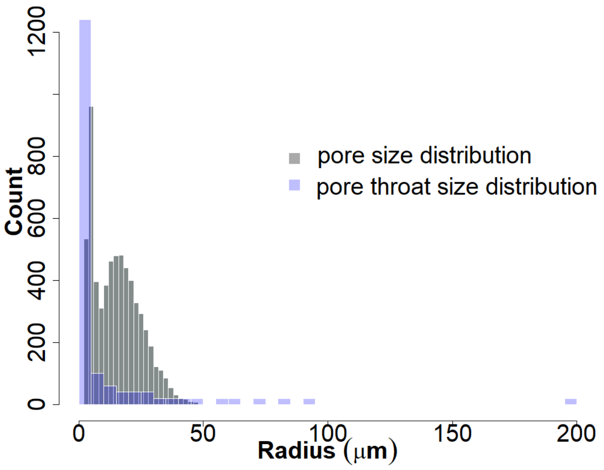

Fig. 2. µCT-derived pore size distribution (grey) and MICP-derived pore throat size distribution (transparent blue). Note that MICP derived counts were multiplied by a factor of 20 to facilitate visualization of the results. All plots used a bin size of 30.

The µCT-evaluated porosity of the Clashach sandstone from the segmented volume of the water-saturated rock was 12.5% to 13.5%, depending on the imaged region of the rock core. The MICP-evaluated pore throat size distribution showed a large number of very small pore throats with <5 µm radius and a small number of small to intermediate size pore throats (>5 to 90 µm) (Fig. 2). The largest pore throat had a radius of 195 µm (Fig. 2). The µCT-evaluated size distribution of the pores evidenced a narrow pore size distribution with comparably small pores with radii <50 µm (Fig. 2, 4a).

3.2 Hydrogen wetting behaviour and stability in UoE experiments

Hydrogen sat in the centre of the pore bodies. Residual brine sat in corners, pore throats (Fig. 3b and c) and, as a subtraction of the water saturated scan from the H_2-and brine filled rock revealed, in thin films around the grains (Fig. 3d). The injected H_2 remained stable within the pore volume under no-flow conditions and at constant pore fluid pressure over a time period of 10 hours which was the maximum experimental duration (SI Fig. S2).

3.2 Effect of pore fluid pressure on hydrogen connectivity, saturation and recovery

Hydrogen saturation during drainage was independent of the pore fluid pressure with 49.8%, 51.7% and 39.7%-52.6% saturation at pore fluid pressures of 2, 5 and 7 MPa, respectively (Fig. 4a-c, f, SI Fig. S3). Hydrogen connectivity during drainage generally showed one large,

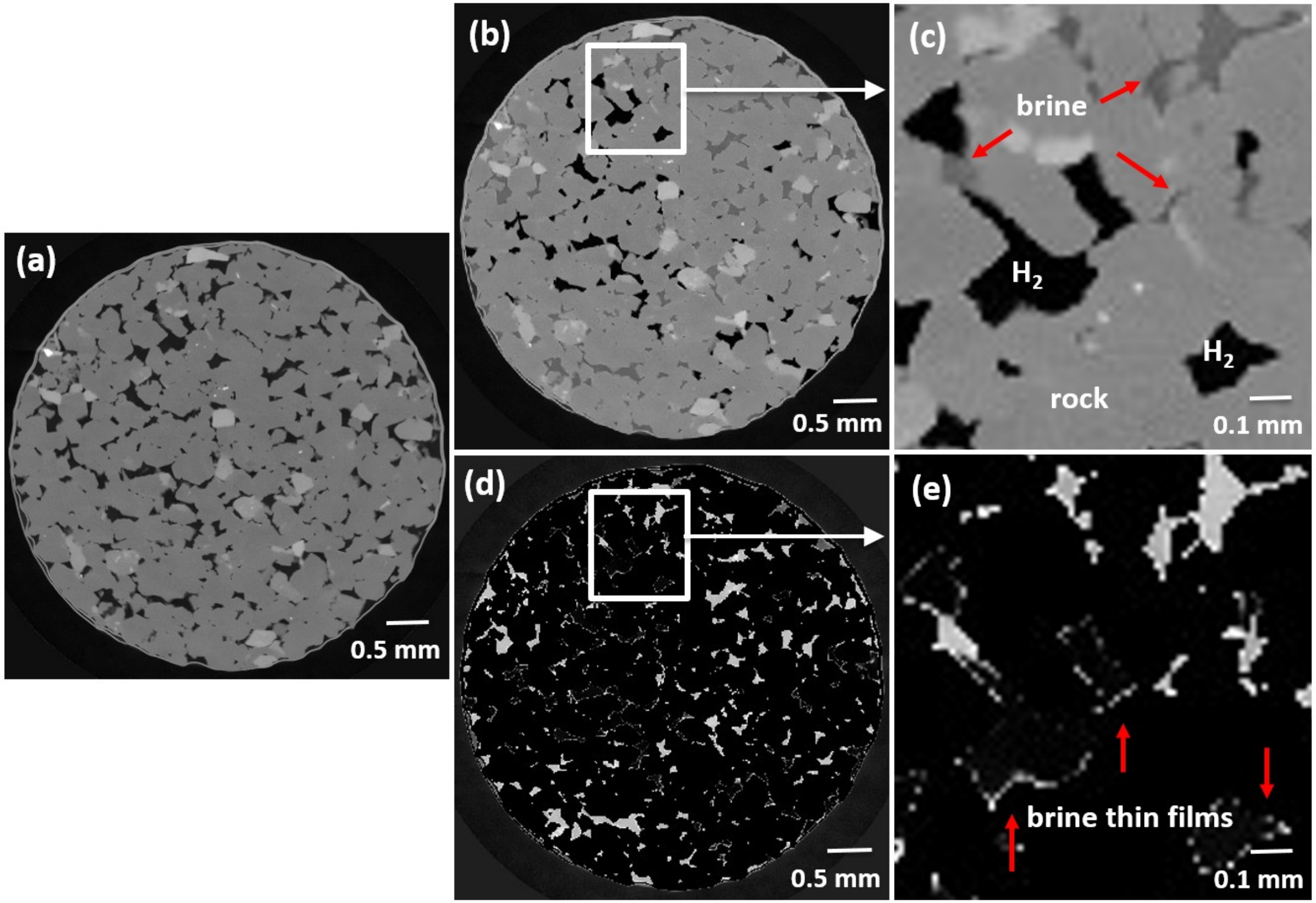

Fig. 3: **(a)** Water-saturated Clashach sandstone with the water shown in black and the rock in different shades of grey. **(b)** and **(c)** Brine-saturated Clashash sandstone after injection of H_2. H_2 (black) fills the centre of the pores while the brine (dark grey) remains in corners and small pore throats around grains. **(d)** and **(e)** Subtraction of the water-wet scan from the brine-saturated scan after H_2 injection, following registration of the brine-saturated scan after H_2 injection to the water-saturated scan, revealing discontinuous brine thin films around grains. The rim around the Al foil in **(d)** is caused by continued shrinkage of the Al foil onto the rock during the experiments.

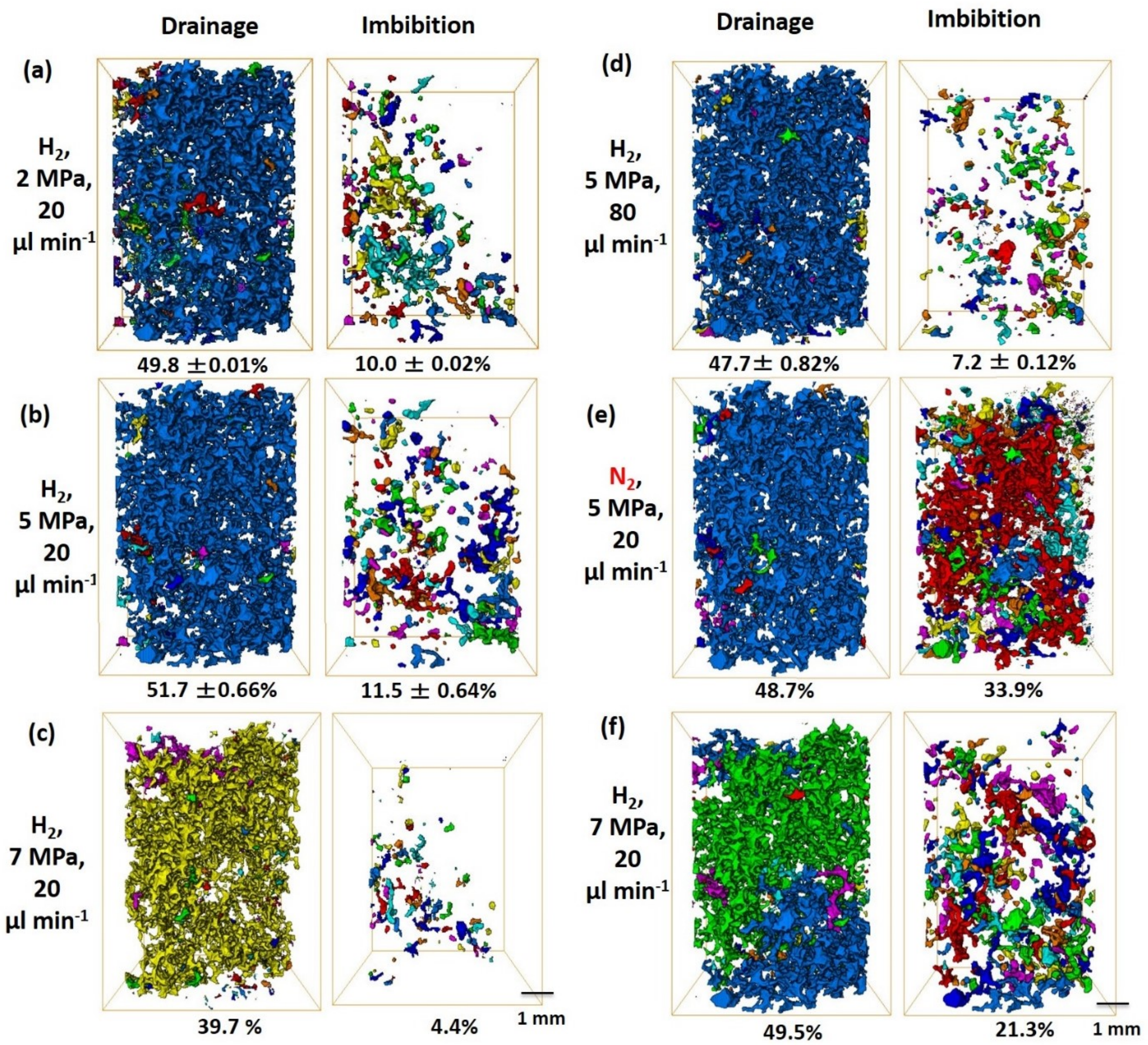

Fig. 4: 3D rendering of H_2 and N_2 clusters with saturation percentages in UoE experiments. Discrete clusters were rendered in colours, where mainly one color marks one large, connected cluster and different colors indicate several, not connected clusters. **(a-c)** Effect of pore fluid pressure on H_2 clusters and saturation after drainage and after primary imbibition. **(a)** 2 MPa, **(b)** 5 MPa and **(c, f)** 7 MPa, all at a constant flow rate of 20 µl min^{-1} corresponding to capillary numbers of 1.7x10^{-8} and 2.4x10^{-6}, respectively. Large, connected clusters that existed after drainage were broken down to numerous smaller clusters after imbibition, with apparently no clear relationship between H_2 saturation and pore fluid pressure. Experiments were repeated once at 2 and MPa, and at 7 MPa twice for drainage runs and once for imbition. For experiments at 2 MPa and 5 MPa averages and standard errors for the H_2 saturation are reported. For experiments at 7 MPa, due to the discrepancy in the results, both of the full primary drainage and imbibition experiments are visualized in **(c)** and **(f)**. **(d)** Effect of cyclic injections on H_2 clusters and saturation: Averages and standard errors of the H_2 saturation after primary and secondary drainage, and after primary and secondary imbibition, all at 5 MPa pore fluid pressure and a flowrate of 80 µl min^{-1} corresponding to a capillary number of 9.4x10^{-6}. **(e)** Nitrogen clusters and saturations during drainage and imbibition at 5 MPa pore fluid pressure and a flowrate of 20 µl min^{-1}. For the full display of the results see SI Fig. S3 and SI Fig S4.

connected cluster at all pore fluid pressures except for one out of three images at 7 MPa which showed three large disconnected clusters (Fig. 5, SI Fig. S3). During drainage, the largest H_2 cluster had a volume of 1x10^8 μm^3 at all pore fluid pressures except for the one run at 7 MPa with the disconnected clusters were the largest volume was 7x10^7 μm^3 (Fig. 5e).

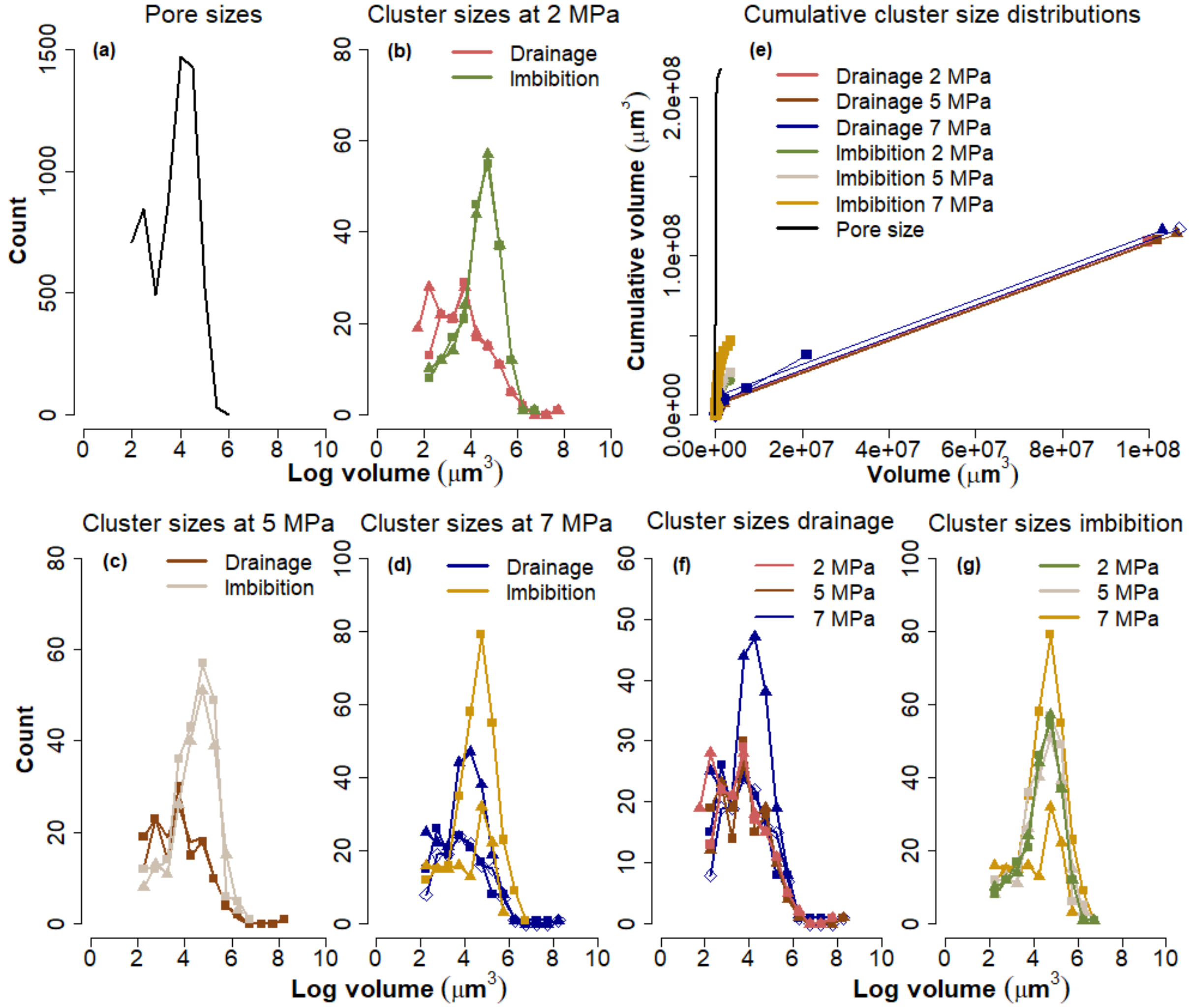

Fig. 5: **(a)** Pore size distribution as derived from the micro-CT image of the water-wet rock. Hydrogen cluster size distributions after drainage and imbibition in experiments at 20 µl min^{-1} flowrate and pore fluid pressures of 2 MPa **(b)**, 5 MPa **(c)** and 7 MPa **(d)**, and cumulative pore size and H_2 cluster size (CS) distributions at different pore fluid pressures **(e),** where squares, triangles and rhombi mark the distinct repeat experiments. **(f)** Hydrogen cluster size distribution after drainage for all experiments and **(g)** Hydrogen cluster size distribution after imbibition for all experiments. Note the large H_2 clusters of ~10^8 μm^3 that exist after drainage in **(b)**-**(d)**. A decrease in the biggest cluster volume after imbibition in **(b)**-**(d)** along with an increase in the number of small clusters marks the change in H_2 structure during the drainage and imbibition processes. Histogram plots in **(a)**-**(d)**, **(f)** and **(g)** used a bin size of 10.

Hydrogen clusters during drainage were at all pore fluid pressures much larger than discrete pores with a maximum volume of 1.3x10^6 µm^3 (Fig. 5e, a). Comparing all H_2 cluster size distributions during drainage (Figure 5f) reveals that all drainage curves, including two of the distributions at 7 MPa (squares and rhombi), have largely the same distribution, however one of the three distributions at 7 MPa (triangles) is distinct. This outlier experiment corresponds to the experiment showing a lower S_{nwi} (Fig. 4c).

Capillary trapping of H_2 during imbibition seemed independent of the pore fluid pressure with 10%, 12% and 4-21% of trapped H_2 at 2, 5 and 7 MPa, respectively (Fig. 4a-c,f, SI Fig. S3), corresponding to 20%, 22% and 11-43% of the initially injected H_2. During imbibition, large H_2 clusters were broken down into smaller clusters (Fig. 5a-d), in line with the visual changes of the H_2 clusters (Fig. 4a-c and f). The largest H_2 clusters after imbibition remained above the maximum pore size during all experiments except for one experiment at 7 MPa (triangles in Fig. 5g, Fig. 5a), showing that not only was H_2 trapped in discrete pore bodies but also as larger H_2 ganglia. The break-down of the largest H_2 clusters during imbibition caused the number of clusters in the size range log 4 to log 6 µm^3 to increase while the number of very small clusters of log 2-4 µm^3 typically decreased (Figs. 5b-d). Comparing all H_2 cluster size distributions during imbibition (Figure 5g) shows that the distributions at 2 and 5 MPa are largely the same while the imbibition distributions at 7 MPa are distinct.

Injections of H_2 and brine into the same rock volume and at the same flow rates and pore fluid pressures of 2-5 MPa were repeatable with small standard errors between 0.01-0.66% (Fig. 4a and b, Fig. 5b and c). At 7 MPa very distinct S_{nwi} and S_{nwr} were measured (Fig. 4c and f); During drainage the standard error was 4.8% at an average H_2 saturation of 47.4%. The standard error during imbibition was 8.5% at an average saturation of 12.9%. The pressure differences between inlet and outlet during these experiments were within the error of the pressure sensors of 0.1% full-scale.

3.3 Effect of hydrogen/brine injection ratio on hydrogen connectivity and saturation

We studied the effect of the H_2 /brine injection ratio on the H_2 saturation in order to evaluate the effect of H_2 injection into hydrodynamic aquifers, and to evaluate what happens in the far field, where fluids will be moving together. The results showed that the H_2 saturation and H_2 interconnected pore volume increased with increasing H_2/brine injection ratio from 32.6% at 4 µl min^{-1} H_2 plus 16 µl min^{-1} brine to 43.2% at 16 µl min^{-1} H_2 plus 4 µl min^{-1} brine (Fig. 6). The H_2 clusters in simultaneous injection experiments occupied many of the same pore spaces as the clusters after H_2 in the non-steady state experiments at the same pressure and total flowrate (Fig. 4b, Fig. 6, SI Fig. S5), and even at the lowest H_2 brine injection ratio of 4 µl min^{-1} H_2 plus 16 µl min^{-1} brine, the H_2 clusters were large, and spanning multiple pores. The percolation threshold, i.e. one connected path from inlet to outlet, was apparently only reached at 100% H_2 injection (Fig. 4b vs. Fig. 6, SI Fig. S5). The pressure

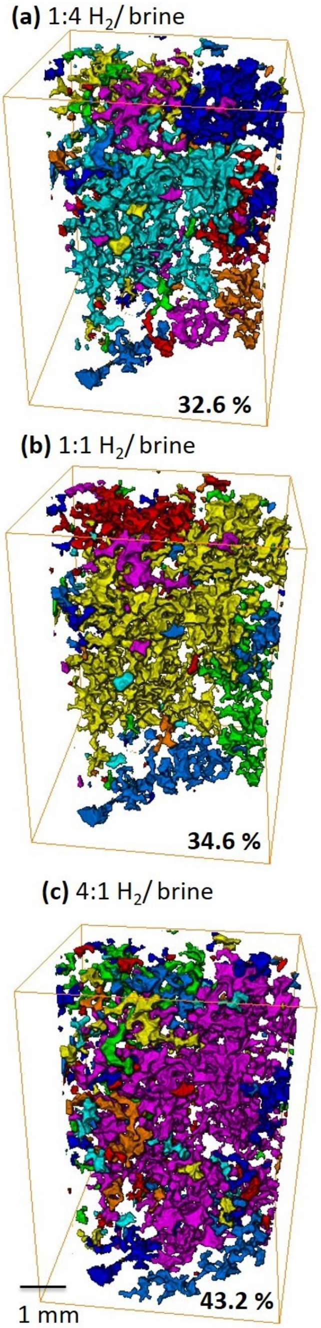

Fig. 6: Effect of H_2/brine injection ratio on H_2 saturation and H_2 connectivity during simultaneous H_2 and brine injection at 5 MPa **(a)** 4 µl min^{-1} H_2 plus 16 µl min^{-1} brine, **(b)** 10 µl min^{-1} H_2 plus 10 µl min^{-1} brine, **(c)** 16 µl min^{-1} H_2 plus 4 µl min^{-1} brine. Discrete H_2 clusters were rendered in colours, where mainly one color marks one large, connected cluster and different colors indicate several, not connected clusters. With increasing injection ratio H_2 saturation and H_2 connectivity increase.

differences between inlet and outlet during the simultaneous injection experiments were up to 0.05 MPa.

The H_2 cluster volume distributions were similar at different H_2:brine injection ratios (Fig. 7a). However, with increasing ratio the smallest H_2 clusters of volume ~log 2 μm^3 decreased in number while the number of intermediate size (log 2.5 to log 6.25 μm^3) H_2 clusters and the volume of the biggest cluster increased (Fig. 7a), confirming observations of increasing H_2 saturation and connectivity with increasing injection ratio (Fig. 6).

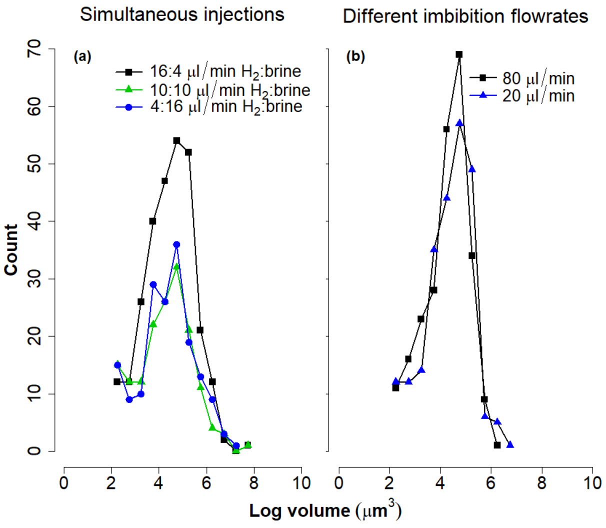

Fig. 7. **(a)** H_2 cluster size distributions during simultaneous injections of H_2 and brine at flowrate ratios of 16:4, 10:10 and 4:16 μl min^{-1} H_2:brine and 5 MPa injection pressure. As the flowrate ratio of H_2 to brine increased, the number of intermediate size H_2 clusters increased and the radius of the biggest cluster increased. **(b)** Effect of flowrate during brine imbibition. All plots used a bin size of 10.

3.4 Effect of flowrate on hydrogen saturation and recovery

At constant pore fluid pressure of 5 MPa, increases in the flowrate during drainage from 20 μl min^{-1} to 80 μl min^{-1}, corresponding to bulk N_C of 1.7 x10^{-8} to 6.8x10^{-8}, respectively, decreased the H_2 saturation from to 51.7% to 47.7% (Figure 4b and d). Correspondingly, increases in the brine flowrate during imbibition from 20 μl min^{-1} to 80 μl min^{-1}, corresponding to bulk N_C of 2.4x10^{-6} and 9.4x10^{-6}, respectively, reduced the S_{nwr} from 11.5% to 7.2% (Fig. 4b and d). In line with this, the H_2 cluster size distributions at the two flowrates showed that larger clusters were mobilized at 80 μl min^{-1} (maximum cluster sizes of log 6.25 μm^3 at 80 μl min^{-1} vs. log 6.75 μm^3 at 20 μl min^{-1}; Fig. 7b). At both flowrates the largest H_2 clusters were still bigger than the largest pore of <log 6 µm^3 (Fig. 7b vs. Fig 6a), indicating that H_2 was trapped also as larger ganglia.

3.5 Secondary drainage and imbibition

Secondary drainage and imbibition did not significantly change the H_2 saturation (47.9% and 7.0%) compared to primary drainage and imbibition (47.6% and 7.3%), based on results at 5 MPa and 80 µl min^{-1} flowrate (SI Fig. S4, Fig. 4d-e).

3.6 Dry rock experiment

In the dry-rock experiment, the brine entered the H_2-filled dry rock via piston-like displacement, (Fig. 8b), eventually recovering the H_2 entirely (Fig. 8d). Before all H_2 was recovered, there was an intermediate stage where previously brine-filled pores (Fig. 8b) showed several very small H_2 bubbles (Fig. 8d).

3.7 Comparison to nitrogen

The N_2 saturation was similar to the H_2 saturation during drainage (48.7% vs. 51.7 ± 0.66%, respectively) but N_2 saturation after brine imbibition was much higher (33.9% vs. 11.5 ± 0.64%, respectively; Fig. 4e, SI Fig. S6). The N_c of H_2 and N_2 during drainage were 1.7×10^{-8} and 3.5×10^{-8}, respectively.

4. Discussion

4.1 Pore space

The µCT-evaluated porosity of the Clashach sandstone from the segmented volume of the water-saturated rock of 12.5-13.6% was within the range of the published porosities of 11.1-14.4% for Clashach sandstone[42-44]. The distributions of pore size and pore throat size as evaluated by µCT and MICP, respectively, suggested that mostly small pores of <50 µm radii were joined by very small throats of <5 µm radii with a few small to intermediate size throats

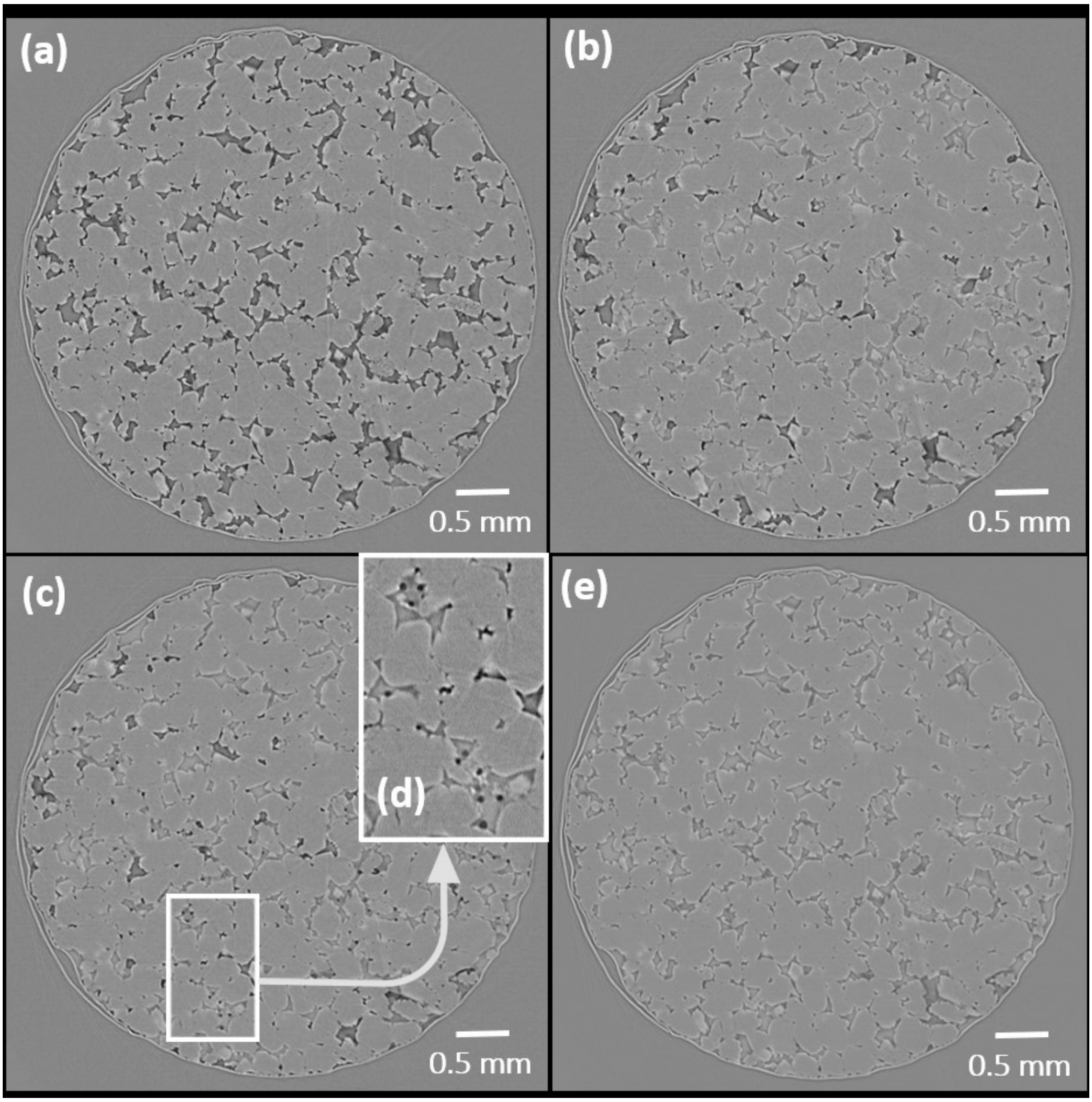

Fig. 8. The dry-rock experiment summarized. **(a)** H_2-saturated, dry rock, **(b)** scan during brine imbibition shortly after appearance of the first brine in the rock, **(c)** scan during brine imbibition after 115 minutes, with several small, isolated H_2 bubbles inside pore bodies **(d),** and **(e)** brine-saturated rock after two hours of imbibition showing 100% recoverability of H_2.

of >5 to 90 μm radii in between (Fig. 2). The largest pore throat of 195 μm radius was probably measured at the surface of the rock core where the drilling process affected the pore space. The pore throat distribution for our Clashach sandstone sample was very similar to the pore throat distribution for Berea sandstone[54]. Compared to the pore throat distributions for Bentheimer sandstone and Doddington sandstone[54], our Clashach sandstone sample showed smaller pore throat sizes. Limestones generally show a wider pore throat size distributions than sandstones[54].

4.2 H_2 flow behaviour and trapping mechanisms

Hydrogen behaved as a non-wetting phase, filling the centre of the pores, with residual brine in the pore corners and throats (Fig. 3b and c), indicating a water wetting system. The largest H_2 cluster was much larger than discrete pores at any pore fluid pressure during drainage (Fig. 5), indicating a good connectivity of the H_2[55]. Hydrogen trapping occurred via snap-off of H_2 ganglia (Fig. 9). Snap-off competes with piston-like, i.e. pore-filling, displacement during the displacement of a non-wetting fluid by a wetting fluid in porous media[21], and is known as the swelling of water in the corner layers of a pore throat during water invasion in water-wet porous rocks until the threshold capillary pressure is exceeded, resulting in spontaneous filling of the throat with water and disconnection of the non-wetting phase which can lead to trapping[21]. Brine films around grains were not directly visible in the tomographic images (Fig. 3b and c)

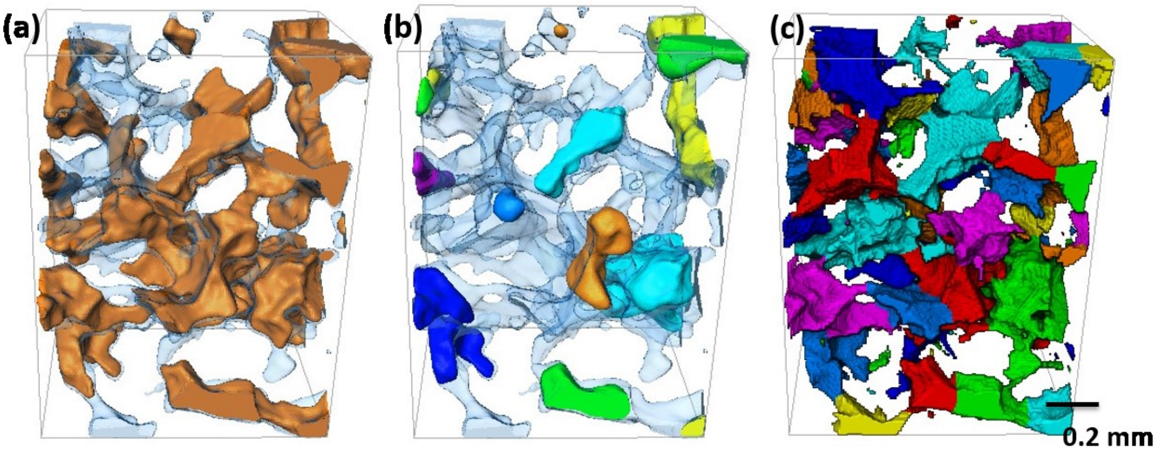

Fig. 9: Example of a snap-off event. **(a)** Labelled H_2-filled volume after drainage (orange), spanning over several pores, and total pore space (transparent blue) showing one large interconnected H_2-filled pore volume. **(b)** Labelled H_2-filled volume after brine imbibition (different coloured shades) and the total pore space (transparent blue) showing several, not connected H_2 ganglia and the snapped-off H_2 droplet (cobalt blue) in the centre, left hand side. **(c)** Pore body visualisation of the same volume.

but were revealed by subtraction of the water-saturated scan from the brine-saturated scan after H_2 injection, following the registration of the brine-saturated scan after H_2 injection to the water-wet scan (Fig. 3d and e). Figures 3d and 3e suggest that brine films were discontinuous and very thin. When H_2 was injected into a dry rock, 100% of the injected H_2 could be recovered (Fig. 8e) which substantiated the theory that sub-resolution brine films around grains and snap-off of H_2 ganglia caused decreased H_2 recovery in experiments using an initially brine saturated rock (UoE experiments). The occurrence of several very small H_2 bubbles in the dry-rock experiment (Fig. 8d) indicated Roof snap-off[56] of H_2 ganglia.

4.3 Effect of pore fluid pressure and hydrogen/brine injection ratio

We observed no dependence of the H_2 saturation during drainage on pore fluid pressure, considering that 2 out of 3 experiments at 7 MPa showed the same the same H_2 saturation of ~50 % as at 2 and 5 MPa (Fig. 4a-c,f, and SI Fig. S3). The one experiment at 7 MPa which had only 39.7% H_2 saturation (Fig. 4c, SI Fig. S3 and blue triangles in Fig. 5f) did also not have the same H_2 cluster size distribution as the remaining experiments (Fig. 5f), despite using the same experimental settings as for all other experiments at 7 MPa, and the log archives of the pore fluid pressures and injected volumes revealed no abnormalities. A shift in the distribution of cluster sizes can indicate a change in wettability, regardless of the measured H_2 saturation. Yet, as two of the results at 7 MPa showed a similar distribution as at the other pressures, it seems likely that this experiment is an outlier. The experiment was acquired after a filament change on the µCT apparatus, which implied that a slightly different part of the same rock core was imaged (13.6% vs. 12.5% porosity). Yet, in principle this should not have affected the results significantly, and subsequent experiments did return to show ~50% H_2 saturation, e.g. the H_2 stability experiment (SI Fig. S2).

The observed constant drainage H_2 saturations with increasing pore fluid pressures from 2 to 7 MPa are in line with a lack of a dependence of the H_2 wettability on pressure increases from 2-

10 MPa in Berea and Bentheimer sandstone[18], with only very small increases of ~3-6° in the H_2 contact angles at pressure increases from 2 to 7 MPa in Basalt[21] and clay[24] and quartz[19], and with a previous findings of no change in the characteristic trapping curves for CO_2 and N_2 at a wide range of pressure and temperature conditions[35]. The general anticipation of an increase in gas saturation with injection pressure[57, 58] may still be valid over pressure ranges larger than the one investigated here. At unchanged wettability, the S_{nwi} is controlled by the capillary pressure which in turn is controlled either by the fractional flow (during simultaneous injection) or by the viscous force pressure drop (during single fluid phase injection). Thus, the independence of the S_{nwi} from the pore fluid pressure indicates that the viscous pressure drop is not being significantly altered by the changing pressure, e.g., the H_2 viscosity change is not having a major impact on the force required to drive flow. Significant loss of H_2 from the gas phase at higher pressures by dissolution into the brine is precluded by the low solubility of H_2 of ~0.02 mol kgw^{-1} at 2.5 MPa[59]. The H_2 stability experiments showed that H_2 saturation at 5 MPa did not change over a time period of ten hours (49.55% at time zero vs. 49.53% ten hours after; SI Fig. S2), evidencing a stable result and no H_2 loss by dissolution.

Looking at the S_{nwr} data only (Fig. 4a-c,f), there was no clear dependency on pore fluid pressure during imbibition. Any change may, however, have been masked by the high variation between the two results at 7 MPa (4-21% Fig. 4c and f). Considering that the experiment at 7 MPa with the low S_{nwi} of 40% could be identified as an outlier (see the discussion in the beginning of section 4.3, and Fig. 5f, blue triangles) and that the S_{nwr} is a function of the S_{nwi} where a lower S_{nwi} will tend to overestimate recovery[54, 60], we may disregard the S_{nwr} of 4%. The large increase in trapped H_2 in the second full primary drainage and secondary imbibition experiment at 7 MPa (Fig. 4f) was probably due to the poorer intial H_2 connectivity[60]. The H_2 cluster size distribution for this experiment showed an increase in the number of intermediate size clusters compared to the other experiments (Fig. 5g, darkyellow squares), without however shifting the cluster distribution, suggesting no wettability change. This indicates that variation in one or more of the other thermophysical properties –density, viscosity, or IFT – have resulted in the impact on the pore scale fluid configuration (Figure 10). Meanwhile, a poorer initial H_2 connectivity was not confirmed by the third repetition of primary drainage at 7 MPa (SI Fig. S3g). More experiments at 7 MPa are needed to confirm the result of increased trapping at higher pore fluid pressures.

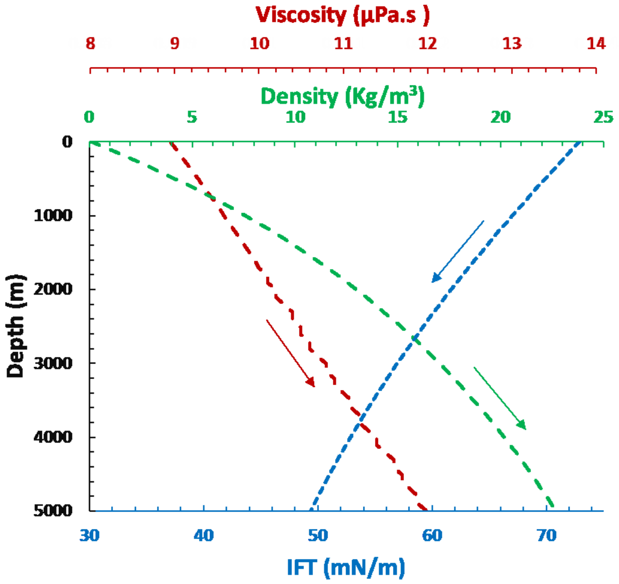

Fig. 10: Density (green line), viscosity (red line), and interfacial tension (blue line) of hydrogen versus depth (Hassanpouryouzband et al. 2021)[61].

Given a hydrostatic gradient of ~10 MPa/km an increase of the S_{nwr} with increasing pore fluid pressure, as suggested by the second experiment at 7 MPa (Fig. 4f), would indicate that deeper aquifers are less favourable for H_2 storage operations. However, unlike our non-steady state experiments which showed barely any pressure difference between inlet and outlet, in a real H_2 storage operation, the well pressure is significantly higher than the reservoir pressure and the brine is not injected, but naturally flowing into previously H_2-saturated rock when the H_2

is recovered- again due to a pressure difference. Our displacement study results are hence applicable to the fringe of the H_2-saturated zone, only, where pressure differences are very small. A decreased H_2 recovery with depth would not align well with other criteria for an economical and safe H_2 storage operation, such as a lower cushion gas requirement with elevated depth[5] and reduced risks for H_2-linked microbial activity at higher depths due to higher temperatures[6].

The pressure/depth effect on our results can be further related to the variation of key pore-scale displacement parameters for H_2 with depth (Fig. 10): The IFT of H_2 reduces with depth whereas the H_2 viscosity increases, both of which in theory should augment the displacement of H_2 with water and reduce the S_{nwr}[62, 63]. However, increased S_{nwr} with decreasing IFT and increasing viscosity has also been demonstrated[64] which may be due to a simultaneously increased likelihood of unstable displacement/ non-uniform fronts[10, 65] during both drainage and imbibition processes at decreasing IFT and increasing viscosity, based on the augmenting effect of both parameters on N_C (Eq. 1). Such unstable displacement processes at higher pore fluid pressures, addition to a variation in the thickness of the brine thin films with pressure, may explain the decrease in interconnected H_2-filled pore volume from one large cluster at 2-5 MPa to three clusters at 7 MPa and have lead to increased snap-off and trapping during imbibition (Fig. 4f).

The S_{nwr} of 10-21% was significantly less than the previously reported H_2 S_{nwr} of 41% for a sandstone under ambient conditions[40]. As mentioned previously, the short length rock sample in Jha et al. (2021)[40] suggests that their results were affected by capillary end effects[46]. However, the applied the relatively high bulk brine N_C of 2.4×10^{-6} may have mobilised more residual H_2 than under strict capillary regime conditions.

During simultaneous injection of H_2 and brine, which may be representative of H_2 injection into hydrodynamic aquifers or simulate the far field conditions, H_2 saturation and H_2

interconnected pore volume increased with increasing H_2/brine injection ratio (Fig. 6). This indicated that a lower brine flow is favoured over high flow environments in terms of optimising the H_2 storage operation. The structure was apparently not percolating in any of the simultaneous injection experiments as opposed to during 100% H_2 injection (Fig. 6 vs. Fig. 4b), yet considering significant pressure differences of up to 0.05 MPa between inlet and outlet in simultaneous injection experiments which were not observed in experiments injecting 100% H_2, the connections between the H_2 clusters may have been broken when the injection (and thereby the pressure gradient) was stopped for the scan.

4.4 Effect of capillary number on initial and residual saturation

Classical pore-scale displacement theory predicts little change in residual phase saturation in response to increases in flow rate until N_C exceeds 10^{-6}-10^{-5}. However, for most subsurface reservoirs there will be rapid decreases at N_C of 10^{-4} or more, when viscous forces become dominant[54]. The bulk brine N_C applied in this study ($2.4\text{-}9.4\text{x}10^{-6}$) was within the range of little saturation change but exceeded the threshold of $N_C < 10^{-6}$ for which the flow generally is said to be capillary dominated[54]. This may indicate that viscous forces caused a significant effect of N_C on the S_{nwr} in our experiments (Fig. 4b and d), and these forces are likely to be even greater at local scale than at bulk[54]. The H_2 cluster size distribution after imbibition at $N_C = 9.4\text{x}10^{-6}$ was shifted with respect to the distribution at $N_C = 2.4\text{x}10^{-6}$ (Fig. 7b), indicating a change in the wetting behaviour and supporting previous findings of preferential desaturation of larger clusters at higher Nc[66].

We observed a 4% decrease in S_{nwi} in our experiments when bulk N_C was increased from $1.7\text{x}10^{-8}$ to $6.8\text{x}10^{-8}$ (Fig. 4b and d). Critical nonwetting phase N_C of $2\text{x}10^{-8}$ and 10^{-5} during imbibition have been reported for water–gas systems and water-oil systems, respectively[67], indicating that the threshold of $N_C < 10^{-6}$ for capillary dominated flow[54] is not rigid. However, considering reported increases in the H_2 saturation after drainage with increasing N_C from

7.7×10^{-7} to 7.7×10^{-5} [20], and acknowledging the small observed difference in S_{nwi}, we cannot exclude that the effect of flow rate was down to experimental variability.

4.5 Comparison to nitrogen

The N_2 saturation was comparable to the H_2 saturation during drainage at similar N_C of $1\text{-}3 \times 10^{-8}$ but the S_{nwr} after imbibition was ~20 % higher for N_2 than for H_2 (Fig. 4b and e). Using N_2 as a proxy for H_2 in experimental drainage and imbibition studies is hence not advisable. Considering the high degree of N_2 trapping, the use of N_2 as a cushion gas for H_2 storage operations which could reduce operational costs[8] seems favourable. Our results are lower than a reported 64% intial N_2 saturation during drainage and 43% residual N_2 saturation during brine (200 g/L NaI +15 g/L $CaCl_2$) imbibition in a Berea sandstone (20-22% porosity) at 5.5 MPa and 20°C[37], and higher than 43% N_2 saturation during drainage in a Bashijiqike tight sandstone (5.6% porosity) at 8 MPa and ambient temperature[36]. The trend in the differences of the N_2 saturation in the above studies follows the same trend as the differences in the porosities of the studied sandstones, with the Clashach sandstone (14% porosity) being intermediate between the two other rocks. This indicates that porosity differences between the different rock types applied in the above experiments defined the observed N_2 saturations, yet differences in the pore throats dimensions may equally have contributed or caused this. Hence S_{nwi} and S_{nwr} depend strongly on (the local conditions within) each rock, and these rock type/local effects may mask any effect of injection conditions. However, trends in the rock-specific behaviour will be controlled by pressure and flow conditions. It follows from this that any rock selected for H_2 storage operations has to be very well characterized, in particular with respect to porosity, turtoisity and capillary pressure curves.

4.6 Suitability of the Clashach sandstone for hydrogen storage

It has been postulated that the low viscosity of H_2 will cause the gas to travel swiftly, making it little suitable for displacing brine[10] and causing low H_2 injectivity. In this work, we showed that from an injectivity and recovery perspective, untreated Clashach sandstone is suitable for underground H_2 storage. However, sandstones aged by exposure to humic acids may be more suitable analogue rocks for experimental investigations of H_2 storage in porous media[19]. Considering that aging has previously been shown to alter the wettability of H_2 brine-quartz systems from highly water-wet toward intermediate-wet[19] the stated H_2 saturations for our untreated outcrop Clashach sandstone are expected to increase during drainage and decrease during imbibition, further the increasing suitability for H_2 storage.

5. Conclusion

In this work, a prima facie examination of H_2 flow and displacement processes in porous rock was carried out as a function of capillary numbers of 1.2-6.8x10^{-8} for H_2 and 2.4-9.5x10^{-6} for brine, and of pore fluid pressures between 2-7 MPa. Results showed no clear relation between pore fluid pressure and H_2 saturation with ~50% of the pore space saturated with H_2 during drainage at all pressures, and 20%, 24% and 43% of the initial H_2 trapped at 2, 5 and 7 MPa, respectively, during imbibition at a capillary number of 2.4x10^{-6}, indicating that higher pressure, i.e. deeper reservoirs are less favourable for H_2 storage. Injection of brine at higher capillary numbers reduced capillary trapping and increased H_2 recovery. Hydrogen recovery was distinct from N_2 recovery, suggesting that N_2 is a poor proxy for H_2. Based on these results, we recommend more shallow, lower pressure sites for future H_2 storage operations in porous media. Future work should aim to measure the influence of pressures above 7 MPa, elevated temperatures and rock aging on H_2 and brine displacement processes at a range of different capillary numbers. Dynamic experiments using synchrotron light sources are recommended to examine displacement mechanisms closely.

Author Contributions

The experimental kit was built by Butler and Thaysen. Experiments were carried out by Thaysen, Butler, Hassanpouryouzband, Freitas. Alvarez-Borges, Atwood and Humphreys were the supporting beamline scientists during the experiments at Diamond Light Source. Image reconstruction and tomographic analysis was carried out by Thaysen. Interpretation of the results was by Thaysen, Butler, Hassanpouryouzband, Krevor and Heinemann. The manuscript was written by Thaysen with review by Butler, Krevor Heinemann, Hassanpouryouzband, Freitas and Edlmann. All authors have given approval to the final version of the manuscript.

Declaration of interest

The authors declare no competing interest.

Funding Sources

Thaysen, Butler, Hassanpouryouzband, Heinemann and Edlmann gratefully acknowledge the funding support from the Engineering and Physical Science Research Council (EPSRC) HyStorPor project [grant number EP/S027815/1] and from the Fuel Cells and Hydrogen 2 Joint Undertaking (JU) under grant agreement No 101006632. The JU receives support from the European Union's Horizon 2020 research and innovation programme and Hydrogen Europe and Hydrogen Europe Research. This work was enabled and carried out with the support of Diamond Light Source, Beamline I12-JEEP 101006632 (proposal mg26730-1).

ACKNOWLEDGMENT

We would like to thank Thomas Connolley for any correspondence and help with setting up the experiments at Diamond Light Source, and Alexis Cartwright-Taylor for assistance and discussions around the experimental results.

References

1. Tarkowski, R., Underground hydrogen storage: Characteristics and prospects *Renew Sust Energ Rev* **2020,** *105*, 86-94.

2. Beckingham, L. E.; Winningham, L., Critical knowledge gaps for understanding water-rock-working phase interactions for compressed energy storage in porous formations. *Acs Sustain Chem Eng* **2020,** *8* (1), 2-11.

3. Mouli-Castillo, J.; Heinemann, N.; Edlmann, K., Mapping geological hydrogen storage capacity and regional heating demands: An applied UK case study. *Appl Energy* **2021,** *283* (116348).

4. Hassanpouryouzband, A.; Joonaki, E.; Edlmann, K.; Heinemann, N.; Yang, J., Thermodynamic and transport properties of hydrogen containing streams. *Sci Data* **2020,** *1* (1), 1-14.

5. Heinemann, N.; Booth, M. G.; Haszeldine, R. S.; Wilkinson, M.; Scafidi, J.; Edlmann, K., Hydrogen storage in porous geological formations - onshore play opportunities in the Midland Valley (Scotland, UK). *Int J Hydrog Energy* **2018,** *43* (45), 20861-20874.

6. Thaysen, E. M.; McMahon, S.; Strobel, G. J.; Butler, I. B.; Ngwenya, B. T.; Heinemann, N.; Wilkinson, M.; Hassanpouryouzband, A.; McDermott, C. I.; Edlmann, K., Estimating microbial growth and hydrogen consumption in hydrogen storage in porous media *Renew Sustain Energ Rev* **2021,** *151* (111481), 1-15.

7. Matos, C. R.; Carneiro, J. F.; Silva, P. P., Overview of large-scale underground energy storage technologies for integration of renewable energies and criteria for reservoir identification. *J. Energy Storage* **2019,** *21*, 241-258.

8. Heinemann, N.; Alcalde, J.; Miocic, J.; Hangz, S. J. T.; Kallmeyer, J.; Ostertag-Henning; Hassanpouryouzband, A.; Thaysen, E. M.; Strobel, G.; Wilkinson, M.; Schmidt-Hattenberger, C.; Edlmann, K.; Bentham, M.; Haszeldine, S.; Carbonell, R.; Rudloff, A.,

Enabling large-scale hydrogen storage in porous media: the scinetific challenges. *Energy Environ Sci* **2021,** *14*, 853-864.

9. Paterson, L., The implications of fingering in underground hydrogen storage. *Int J Hydrogen Energ* **1983,** *8* (1), 53-59.

10. Chaturvedi, K. R.; Bajpai, S.; Trivedi, J.; Sharma, T., Air foams for mobility control and subsurface storage of hydrogen in porous media: An experimental study. *Energy & Fuels* **2022,** *36*, 5036-5046.

11. Flesch, S.; Pudlo, D.; Albrecht, D.; Jacob, A.; Enzmann, F., Hydrogen underground storage-Petrographic and petrophysical variations in reservoir sandstones from laboratory experiments under simulated reservoir conditions. *Int J Hydrog Energy* **2018,** *43* (45), 20822-20835.

12. Yekta, A. E.; Pichavant, M.; Audigane, P., Evaluation of geochemical reactivity of hydrogen in sandstone: Application to geological storage. *J Appl Geochem* **2018,** *95*, 182-194.

13. Hassanpouryouzband, A.; Adie, K.; Cowen, T.; Thaysen, E. M.; Heinemann, N.; Butler, I. B.; Wilkinson, M.; Edlmann, K., Geological Hydrogen Storage: Geochemical Reactivity of Hydrogen with Sandstone Reservoirs. *ACS Energy Lett* **2022,** *7*, 2203-2210.

14. Yekta, A. E.; Manceau, J. C.; Gaboreau, S.; Pichavant, M.; Audigane, P., Determination of Hydrogen-Water Relative Permeability and Capillary Pressure in Sandstone: Application to Underground Hydrogen Injection in Sedimentary Formations. *Transport Porous Med* **2018,** *122* (2), 333-356.

15. Rezaei, A.; Hassanpouryouzband, A.; Molnar, I.; Derikvand, Z.; Haszeldine, R. S.; Edlmann, K., Relative permeability of hydrogen and aqueous brines in sandstones and carbonates at reservoir conditions. *Geophys Res Lett* **2022**.

16. Higgs, S.; Da Wang, Y.; Sun, C.; Ennis-King, J.; Jackson, S. J.; Armstrong, R. T.; Mostaghimi, P., In-situ hydrogen wettability characterisation for underground hydrogen storage. *Int J Hydrog Energy* **2021,** *47* (26), 13062-13075.

17. Esfandyari, H.; Sarmadivaleh, M.; Esmaeilzadeh, F.; Ali, M.; Iglauer, S.; Keshavarz, A., Experimental evaluation of rock mineralogy on hydrogen-wettability: Implications for hydrogen geo-storage. *J Energy Storage* **2022,** *52* (104866), 1-8.

18. Hashemi, L.; Glerum, W.; Farajzadeh, R.; Hajibeygi, H., Contact angle measurement for hydrogen/brine/sandstone system using captive-bubble method relevant for underground hydrogen storage. *Adv Water Resour* **2021,** *154* (103964), 1-13.

19. Iglauer, S.; Muhammad, A.; Keshavarz, A., Hydrogen wettability of sandstone reservoirs: implications for hydrogen geo-storage. *Geophys Res Lett* **2020,** *48* (3), 1-5.

20. Lysyy, M.; Ersland, G.; Fernø, M., Pore-scale dynamics for underground porous media hydrogen storage. *Adv Water Resour* **2022,** *163* (104167), 1-13.

21. Al-Yaseri, A.; Jha, N. K., On hydrogen wettability of basaltic rock. *J Pet Sci Eng* **2021,** *200*, 1-5.

22. Hosseini, M.; Ali, M.; Fahimpour, J.; Keshavarz, A.; Iglauer, S., Basalt-H_2-brine wettability at geo-storage conditions: Implication for hydrogen storage in basaltic formation. *J Energy Storage* **2022,** *52* (104745), 1-6.

23. van Rooijen, W.; Hashemi, L.; Boon, M.; Farajzadeh, R.; Hajibeygi, H., Microfluidics-based analysis of dynamic contact angles relevant for underground hydrogen storage. *Adv Water Resour* **2022,** *164* (104221), 1-17.

24. Al-Yaseri, A.; D., W.-B.; Fauziah, C. A.; Iglauer, S., Hydrogen wettability of clays: Implications for underground hydrogen storage. *Int J Hydrog Energy* **2021,** *46* (69), 34356-34361.

25. Azin, R.; Izadpanahi, A., *Fundamentals and practical aspects of gas injection* Springer: 2022.

26. Morrow, N.; Chatzis, I.; Taber, J. J., Entrapment and mobilization of residual oil in bead packs. *SPE Reservoir Engineering* **1988,** *3* (3).

27. Blunt, M. J.; Bijeljic, B.; Dong, H.; Gharbi, O.; Iglauer, S.; Mostaghimi, P.; Paluszny, A.; Pentland, C. H., Pore-scale imaging and modelling. *Adv Water Resour* **2013,** *51*, 197-216.

28. Saraf, S.; Bera, A., A review on pore-scale modeling and CT scan technique to characterize the trapped carbon dioxide in impermeable reservoir rocks during sequestration. *Renew Sust Energ Rev* **2021,** *144* (110986), 1-20.

29. Xu, L.; Myers, M.; Li, Q.; White, C.; Zhang, X., Migration and storage characteristics of supercritical CO_2 in anisotropic sandstones with clay interlayers based on micro-CT experiments. *J Hydrol* **2020,** *580* (124239), 1-17.

30. Iglauer, S.; Paluszny, A.; Pentland, C. H.; Blunt, M. J., Residual CO_2 imaged with x-ray micro-tomography. *Geophys Res Lett* **2011,** *38* (L21403), 1-6.

31. Andrew, M.; Menke, H.; Blunt, M. J.; Bijeljic, B., The imaging of dynamic multiphase fluid flow using synchrotron-based x-ray microtomography at reservoir conditions. *Tranp Porous Med* **2015,** *110* (1), 1-24.

32. Andrew, M.; Bijeljic, B.; Blunt, M. J., Pore-scale imaging of trapped supercritical carbon dioxide in sandstones and carbonates. *Int J Greenh Gas Control* **2014,** *22*, 1-14.

33. Krevor, S. C. M.; Pini, R.; Zuo, L.; Benson, S. M., Relative permeability and trapping of CO_2 and water in sandstone rocks at reservoir conditions. *Water Resour Res* **2012,** *48*, 1-16.

34. Rahman, T.; Lebedev, M.; Barifcani, A.; Iglauer, S., Residual trapping of supercritical CO_2 in oil-wet sandstone. *J Colloid Interf Sci* **2016,** *469*, 63-68.

35. Niu, B.; Al-Menhali, A.; Krevor, S. C., The impact of reservoir conditions on the residual trapping of carbon dioxide in Berea sandstone. *Water Resour Res* **2015,** *51* (4), 2009-2029.

36. Cao, Q.; Gong, Y.; Fan, T.; Wu, J., Pore-scale simulations of gas storage in tight sandstone reservoirs for a sequence of increasing injection pressure based on micro-CT. *J Nat Gas Sci Eng* **2019,** *64*, 15-27.

37. Khishvand, M.; Alizadeh, A. H.; Piri, M., In-situ characterization of wettability and pore-scale displacements during two- and three-phase flow in natural porous media. *Adv Water Resour* **2016,** *97*, 270-298.

38. Sarmadivaleh, M.; Al-Yaseri, A.; Iglauer, S., Influence of temperature and pressure on quartz–water–CO_2 contact angle and CO_2–water interfacial tension. *J Colloid Interf Sci* **2015,** *441*, 59-64.

39. Al-Yaseri, A.; Esteban, L.; Giwelli, A.; Sarout, J.; Lebedev, M.; Sarmadivaleh, M., Initial and residual trapping of hydrogen and nitrogen in Fontainebleau sandstone using nuclear magnetic resonance core flooding. *Int J Hydrog Energy* **2022,** *in press*.

40. Jha, N. K.; Al-Yaseri, A.; Ghasemi, M.; Al-Bayati, D.; Lebedev, M.; Sarmadivaleh, M., Pore scale investigation of hydrogen injection in sandstone via X-ray micro-tomography. *Int J Hydrog Energy* **2021,** *46*, 34822-34829.

41. Pak, T.; Butler, I. B.; Geiger, S.; van Dijke, M. I. J.; Sorbie, K. S., Droplet fragmentation: 3D imaging of a previously unidentified pore-scale process during multiphase flow in porous media. *P Natl Acad Sci USA* **2015,** *112* (7), 1947-1952.

42. Iglauer, S.; Ferno, M. A.; Shearing, P.; Blunt, M. J., Comparison of residual oil cluster size distribution, morphology and saturation in oil-wet and water-wet sandstone. *J Colloid Interf Sci* **2012,** *375*, 187-192.

43. Iglauer, S.; Paluszny, A.; Blunt, M. J., Simultaneous oil recovery and residual gas storage: A pore-level analysis using in situ X-ray micro-tomography. *Fuel* **2013,** *103*, 905-914.

44. Pentland, C. H.; Tanino, Y.; Iglauer, S.; Blunt, M. J., Capillary trapping in water-wet sandstones: coreflooding experiments and pore-network modeling. In *SPE International* Society of Petroleum Engineers Florence, Italy 2010.

45. Fusseis, F.; Steeb, H.; Xiao, X.; Zhu, W.-l.; Butler, I. B.; Elphick, S.; Maeder, U., A low-cost X-ray-transparent experimental cell for synchrotron-based X-ray microtomography studies under geological reservoir condition. *J Synchrotron Radiation* **2014** *21* (1), 251-253.

46. Pak, T. Saturation tracking and identification of residual oil saturation. University of Edinburgh 2014.

47. Kumar, M.; Sok, R.; Knackstedt, M. A.; Latham, S.; Senden, T. J.; Sheppard, A. P.; Varslot, T.; Arns, C. In *Mapping fluid distributions in 3D at the pore scale: Quantifying the influence of wettability and saturation history on rock resistivity*, SPWLA 50th Annual Logging Symposium, Society of Petrophysicists and Well-Log Analysts: 2009.

48. Yusibani, E.; Nagahama, Y.; Kohno, M.; Takata, Y.; Woodfield, P. L.; Shinzato, K.; Fujii, M., A capillary tube viscometer designed for measurements of hydrogen gas viscosity at high pressure and high temperature. *Int J Thermophys* **2011,** *32* (6), 1111-1124.

49. Chow, Y. T. F.; Maitland, G. C.; Trusler, J. P. M., Interfacial tensions of (H2O + H-2) and (H2O + CO2 + H-2) systems at temperatures of (298-448) K and pressures up to 45 MPa. *Fluid Phase Equilibr* **2018,** *475*, 37-44.

50. Chow, Y. T. F.; Maitland, G. C.; Trusler, J. P. M., Erratum to "Interfacial tensions of (H2O + H-2) and (H2O + CO2 + H-2) systems at temperatures of (298-448) K and pressures up to 45 MPa". *Fluid Phase Equilibr* **2020,** *503* (112315), 1.

51. Nakai, T.; Sawamura, S.; Taniguchi, Y.; Yamaura, Y., Effect of pressure on the viscosity B coefficient of cesium chloride in water *Mater Sci Res Int* **1996,** *2* (3), 143-147.

52. Vlassenbroeck, J.; Masschaele, B.; Cnuddle, V.; Dierick, M.; Pieters, K.; Van Hoorebeke, L.; Jacobs, P., Octopus 8: A high performance tomographic reconstruction package for X-ray tube and synchrotron micro-CT. In *Advances in X-ray tomography for geomaterials*, Desrues, J.; Viggiani, G.; Bésuelle, P., Eds. ISTE: London, UK, 2010.

53. Buades, A.; Coll, B.; Morel, J. M. In *A non-local algorithm for image denoising*, 2005 IEEE Computer Society Conference on Computer Vision and Pattern Recognition (CVPR'05), 2005; pp 60-65.

54. Blunt, M. J., *Multiphase flow in permeable media. A Pore-scale perspective* Cambridge University Press Cambridge, United Kingdom, 2017.

55. Singh, K.; Menke, H.; Andrew, M.; Lin, Q.; Rau, C.; Blunt, M. J.; Bijeljic, B., Dynamics of snap-off and porefilling events during two-phase fluid flow in permeable media. *Sci Rep* **2017,** *7* (5192), 1-13.

56. Roof, J. G., Snap-off of oil droplets in water-wet pores. *Soc Petrol Eng J* **1970,** *10* (1), 85-90.

57. Thomas, L. K.; Katz, D. L.; Tek, M. R., Threshold pressure phenomena in porous media. *Soc Petrol Eng J* **1968**, 174-184.

58. Boone, M. A.; Kock, T. D.; Bultreys, T.; Schutter, G. D.; Vontobel, P.; Hoorebeke, L. V.; Cnudde, V., 3D mapping of water in oolithic limestone at atmospheric and vacuum saturation using X-ray micro-CT differential imaging. *Mater Char* **2014,** *97*, 150-160.

59. De Lucia, M.; Pilz, P.; Liebscher, A.; Kuhn, M., Measurements of H2 solubility in saline solutions under reservoir conditions: preliminary results from project H2STORE. *Enrgy Proced* **2015,** *76*, 487-494.

60. Herring, A. L.; Harper, E.; Andersson, L.; Sheppard, A.; Bay, B. K.; Wildenschild, D., Effect of fluid topology on residual nonwetting phase trapping: Implications for geologic CO_2 sequestration. *Adv Water Resour* **2013,** *62*, 47-58.

61. Hassanpouryouzband, A.; Joonaki, E.; Edlmann, K.; Haszeldine, R. S., Offshore Geological Storage of Hydrogen: Is This Our Best Option to Achieve Net-Zero? *ACS Energy Lett* **2021,** *6* (6), 2181–2186.

62. Wagner, O. R.; Leach, R. O., Effect of interfacial tension on displacement efficiency. *SPE J* **1966,** *6* (4), 335-344.

63. Avraam, D. G.; Payatakes, A. C., Flow Mechanisms, Relative Permeabilities, and Coupling Effects in Steady-State Two-Phase Flow through Porous Media. The Case of Strong Wettability. *Ind Eng Chem Res* **1999,** *38*, 778-786.

64. Cho, J.; Kim, T. H.; Chang, N.; Lee, K. S., Effects of relative permeability change resulting from interfacial tension reduction on vertical sweep efficiency during the CO2-LPG hybrid EOR process. *Energy Sources* **2018,** *40* (10), 1242-1249.

65. Sabet, N.; Hassanzadeh, H.; Abedi, J., Stability of Gravitationally Unstable Double Diffusive Transient Boundary Layers with Variable Viscosity in Porous Media. *Aiche J* **2017,** *63* (6), 2471-2482.

66. Oughanem, R.; Youssef, S.; Peysson, Y.; Bazin, B.; Maire, E.; Vizika, O., Pore-scale to core-scale study of capillay desaturation curves ulti multi-scale 3D imaging In *International Symposium of the Society of Core Analysts*, Napa Valley, California, USA, 2013.

67. Ding, M.; Kantzas, A., Capillary number correlations for gas-liquid systems. *J Can Petrol Technol* **2007,** *46* (27-32).

Supplementary Information

Pore-scale imaging of hydrogen displacement and trapping in porous media

Eike M. Thaysen[2*], Ian Butler[1], Damien Freitas[1], Aliakbar Hassanpouryouzband[1], Fernando Alvarez-Borges[2], Samuel C. Krevor[3], Niklas Heinemann[1], Robert Atwood[2], Katriona Edlmann[1]

[1]School of Geoscience, Grant Institute, The King's Buildings, The University of Edinburgh, James Hutton Road, Edinburgh, EH9 3FE, United Kingdom

[2] Diamond Light Source Ltd, Harwell Campus, Didcot OX11 0DE, UK

[3] Department of Earth Science and Engineering, Imperial College London, London SW7 2AZ, United Kingdom

---

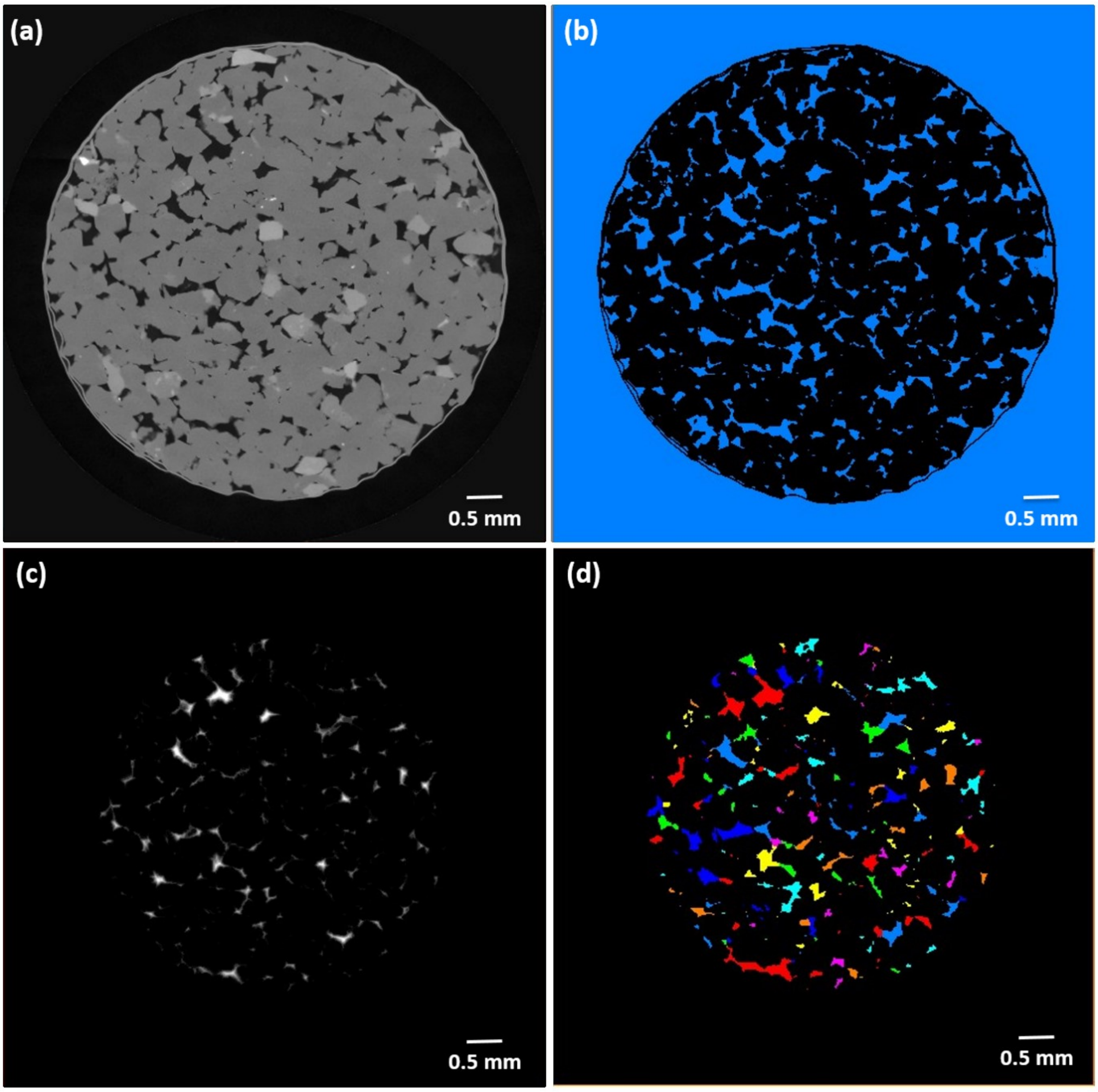

SI Figure S1: Image processing workflow for UoE experiments. **(a)** The image after reconstruction and filtering. **(b)** The image after segmenting using a global threshold. **(c)** The outer part of the rock core touching the Al foil was removed through application of a mask, and a chamfer distance map of the pore space was calculated by assigning each voxel the distance from it to the nearest pore wall. **(d)** This was then used to separate the pore space into individual pores by calculating the water-shed basins of the distance map.

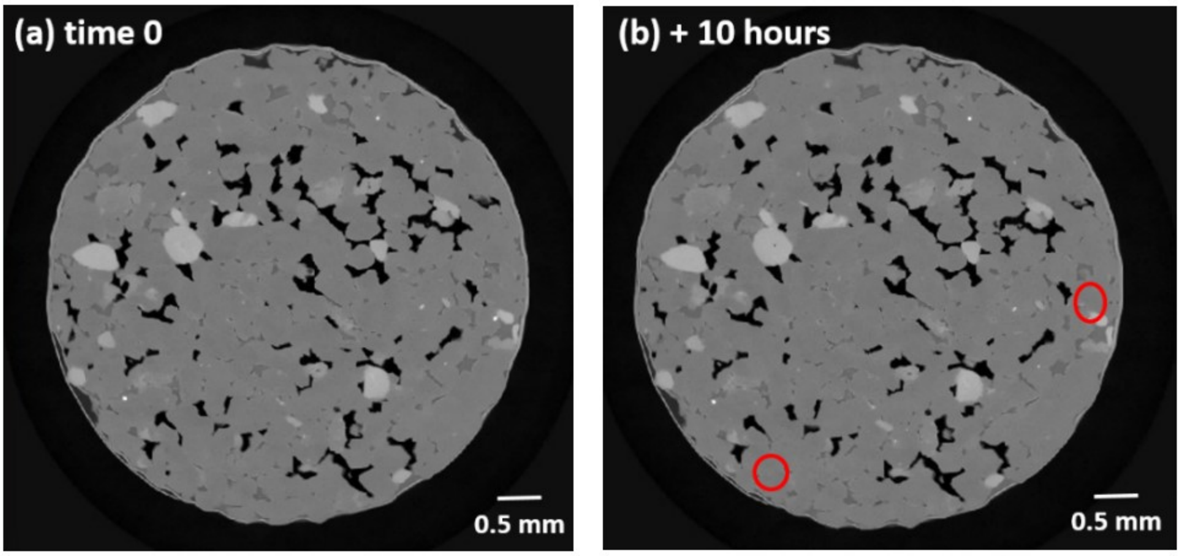

SI Figure S2: H_2 stability at 7 MPa injection pressure and a flow rate of 20 µl min^{-1} (capillary number 2*10^{-8}) at time zero **(a)** and after ten hours **(b)**. Red circles indicate subtle differences in the hydrogen filled pore volume after ten hours. The difference in the hydrogen saturation for the total scanned rock volume was within error at 49.55% % and 49.53% for time 0 and after ten hours, respectively.

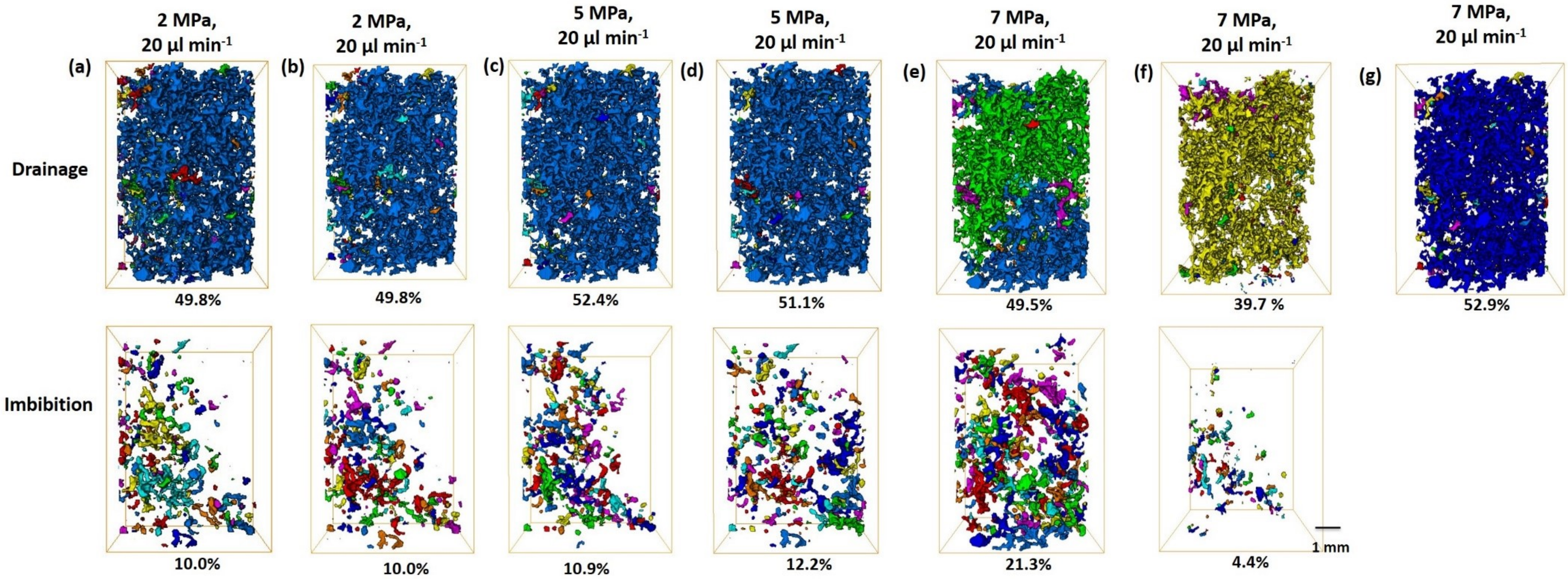

SI Figure S3: Enlarged view of 3D renderings of H_2 with saturation percentages in UoE experiments. Discrete clusters were rendered in colours, where mainly one colour marks one large, connected cluster and different colours indicate several, not connected clusters. **(a-d)** Effect of pore fluid pressure on H_2 clusters and saturation after drainage and after primary imbibition. **(a)** 2 MPa, **(b)** 5 MPa and **(c-e)** 7 MPa, all at a constant flow rate of 20 µl min^{-1} corresponding to capillary numbers of 1.7×10^{-8} and 2.4×10^{-6}, respectively.. Experiments were repeated once. For experiments at 2 MPa and 5 MPa averages and standard errors for the H_2 saturation are reported. For experiments at 7 MPa, due to the discrepancy in the results, both results are visualized **(c-d)**.

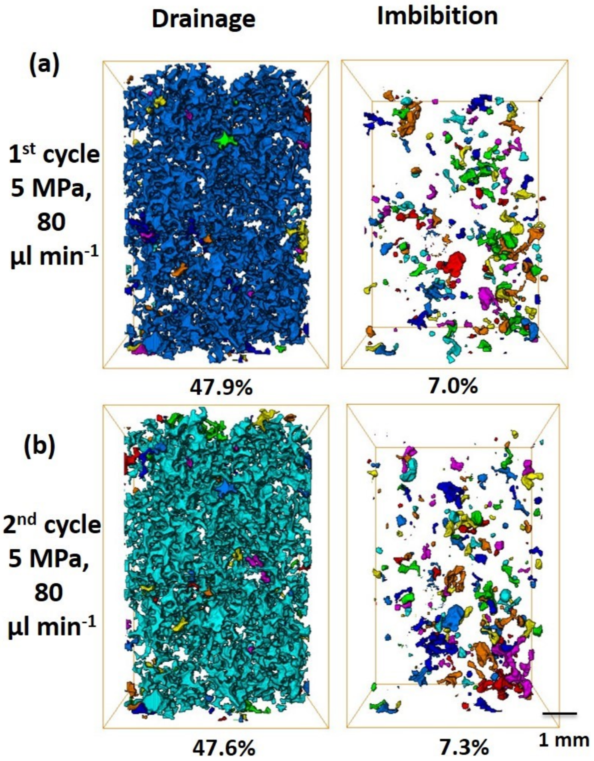

SI Figure S4: Cyclic H_2 injection into Clashach sandstone at 5 MPa and 80 µl min^{-1} corresponding to a capillary number of 9.4x10^{-6}, showing no significant differences in H_2 saturation and H_2 connectivity after primary drainage and imbibition as compared to after secondary drainage and imbibition.

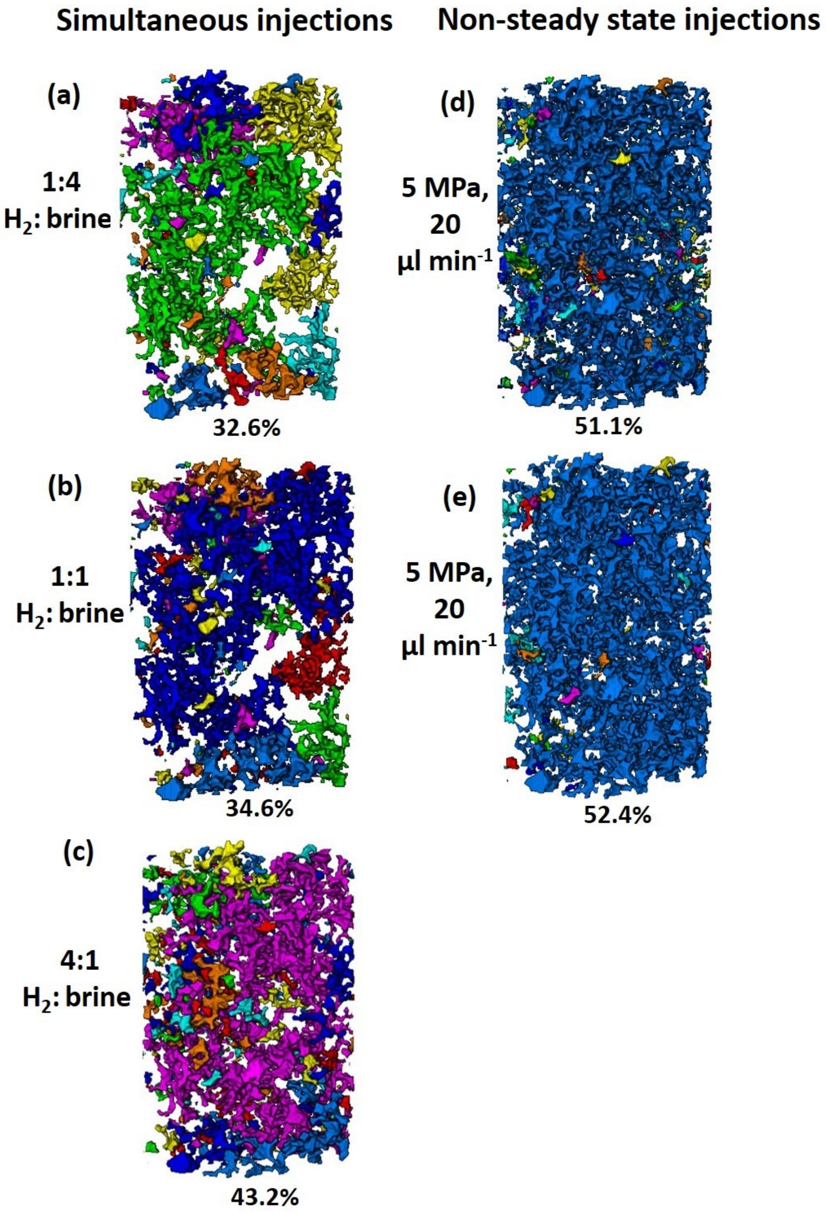

SI Figure S5: Comparison of the distribution of the H_2 clusters in the pore space between simultaneous H_2 and brine injection experiments **(a-c)** and the two repetitions of the non-steady state H_2 injection **(d)** and **(e)**, all at 5 MPa and a total flow rate of 20 µl min^{-1}.

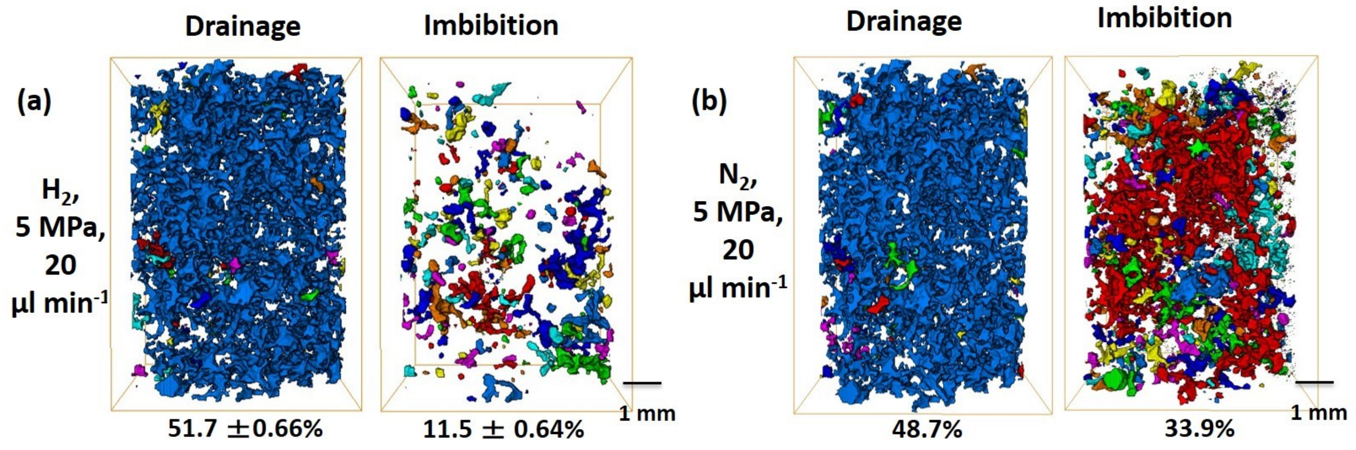

SI Figure S6: Nitrogen clusters and saturations during drainage and imbibition at 5 MPa pore fluid pressure and a flowrate of 20 µl min^{-1}